Langtaosha (LTS) Preprint doi: https://doi.org/10.65215/LTSpreprints.2026.11.24.000400. This version posted November 24, 2026. The copyright holder for this preprint (which was not certified by peer review) is the author/funder. Creative Commons license: CC Attribution-NonCommercial-NoDerivatives 4.0 https://creativecommons.org/licenses/by-nc-nd/4.0

Target-locked volumetric microscopy

Authors

Zichen Ding[1,2]†, Yu Wu[2,3]†, Yun Ling[4]†, Hao Sha[2,5], Yue Hu[1], Haoyu Li[4], Shangguo Hou[2*]

Affiliation

[1]School of Electronics and Information Engineering, Harbin Institute of Technology, Harbin, 150001, China

[2]Systems and Physical Biology Institute, Shenzhen Bay Laboratory, Shenzhen, 518132, China

[3]School of Life Science and Technology, Harbin Institute of Technology, Harbin, 150001, China

[4]School of Instrumentation Science and Engineering, Harbin Institute of Technology, Harbin 150001, China

[5]School of Computer Science and Technology, Harbin Institute of Technology (Shenzhen), Shenzhen, 518006, China

[*]Corresponding author. Email: shangguo.hou@szbl.ac.cn

†These authors contributed equally to this work.

Langtaosha (LTS) Preprint doi: https://doi.org/10.65215/LTSpreprints.2026.11.24.000400. This version posted November 24, 2026. The copyright holder for this preprint (which was not certified by peer review) is the author/funder. Creative Commons license: CC Attribution-NonCommercial-NoDerivatives 4.0 https://creativecommons.org/licenses/by-nc-nd/4.0

Abstract

Dynamic interactions with cellular membranes and organelles govern the cellular fate of biological and synthetic particles, shaping processes from intracellular trafficking and viral infection to therapeutic delivery. Resolving these interactions requires continuous three-dimensional observation of individual moving particles and their evolving surroundings at high spatiotemporal resolution. However, fixed-volume microscopy must balance field of view against acquisition speed and sampling efficiency. Here we introduce single-target adaptive region scanning in three dimensions (STARS), which integrates active-feedback tracking with photon-resolved volumetric imaging through a shared rapid scan of a local volume that follows the target. STARS records three-dimensional trajectories of target at 1-ms intervals with nanometer-scale positional precision while reconstructing the surrounding cellular structures with tunable temporal resolution. We applied STARS to investigate nanoparticle interactions with the plasma membrane, microtubules and lysosomes in live cells. It was further used to resolve spatially heterogeneous nanoparticle motion around a developing membrane protrusion while quantifying protrusion growth from approximately 0.4 to 1.8 μm over 60 s. By shifting volumetric acquisition from a fixed region to the moving target, STARS connects particle trajectories with evolving cellular architecture, enabling transient particle–cell interactions to be examined in a co-moving three-dimensional context and providing a foundation for future adaptive and event-guided imaging.

Langtaosha (LTS) Preprint doi: https://doi.org/10.65215/LTSpreprints.2026.11.24.000400. This version posted November 24, 2026. The copyright holder for this preprint (which was not certified by peer review) is the author/funder. Creative Commons license: CC Attribution-NonCommercial-NoDerivatives 4.0 https://creativecommons.org/licenses/by-nc-nd/4.0

INTRODUCTION

Resolving biological interactions in three dimensions at high spatiotemporal resolution is essential for understanding dynamic cellular processes (*1-4*). Interactions between biological and synthetic particles and cellular structures govern processes ranging from intracellular trafficking and viral infection to therapeutic delivery (*5-9*). Vesicles, viruses, protein assemblies, and synthetic probes move through cells while transiently interacting with membranes, cytoskeletal networks, and organelles (*10-13*). Understanding these interactions requires not only measuring how a particle moves, but also how its motion relates to the surrounding cellular architecture. Although a particle trajectory can reveal changes in mobility and confinement, it cannot identify the local structures associated with these changes. Because these interactions are intrinsically three-dimensional and often occur on subsecond timescales, resolving them requires continuous, high-resolution observation of individual particles and their evolving cellular surroundings.

Maintaining this combined observation is challenging when the region of interest is small and moving. In fixed-volume imaging, reducing the imaging volume increases the risk of losing the moving target, whereas expanding it increases acquisition time and unnecessary illumination of regions outside the immediate area of interest (*1, 14*). Fast confocal, spinning-disk, multifocus, light-field, light-sheet and remote-focusing approaches have substantially increased volumetric acquisition rates (*3, 15-33*), while adaptive and event-driven strategies prioritize selected regions or time periods (*34-43*). On the other hand, active-feedback tracking enables continuous monitoring of particle dynamics by dynamically recentering the excitation volume around the moving target in real time (*44-57*). Active-feedback tracking has been combined with complementary volumetric imaging, as exemplified by 3D-TrIm (*10*). These advances motivate a more focused acquisition strategy: using the same rapid three-dimensional scan both to localize a moving target and to image its immediate surroundings. This strategy would allow the imaging volume to follow the target dynamically, maintaining structural context around the object of interest without repeatedly sampling a large, fixed volume.

We propose that volumetric imaging need not be referenced to a fixed microscope stage. Instead, the moving target itself can serve as the reference frame, allowing its local environment to be imaged continuously as it moves through the specimen. Based on this strategy, we introduce single-target adaptive region scanning in three dimensions (STARS), which uses a shared rapid

Langtaosha (LTS) Preprint doi: https://doi.org/10.65215/LTSpreprints.2026.11.24.000400. This version posted November 24, 2026. The copyright holder for this preprint (which was not certified by peer review) is the author/funder. Creative Commons license: CC Attribution-NonCommercial-NoDerivatives 4.0 https://creativecommons.org/licenses/by-nc-nd/4.0

3D scan for active-feedback tracking and photon-resolved imaging, thereby restricting contextual acquisition to a local volume that dynamically follows the target. STARS enables recording three-dimensional trajectories of target at 1-ms intervals with nanometer-scale positional precision while reconstructing the surrounding cellular structures tunable temporal resolution.

We validate trajectory-guided reconstruction using simulations and fixed samples, and apply STARS to investigate nanoparticle interactions with the plasma membrane, microtubules and lysosomes in live cells. These measurements link changes in nanoparticle mobility to the three-dimensional organization of nearby cellular structures. We further resolve spatially heterogeneous nanoparticle motion around a developing membrane protrusion while quantifying protrusion growth. By shifting volumetric acquisition from a fixed region to the moving target, STARS connects continuous particle trajectories with evolving local architecture, providing a target-centered approach for investigating transient particle–cell interactions in their three-dimensional structural context.

RESULTS

STARS overview

The general workflow of STARS is illustrated in **Fig. 1**. In STARS, a shared three-dimensional excitation scan was used for active-feedback 3D single particle tracking and photon-resolved volumetric imaging of the surrounding volume. Rapid particle localization and volumetric imaging require high-speed three-dimensional excitation scanning, whereas minimizing illumination outside the region of interest demands a confined scanning volume. To meet these requirements, we combined a pair of electro-optic deflectors (EODs) for lateral scanning with a tunable acoustic gradient (TAG) lens for axial scanning (**Fig. 1A** and **fig. S1**). The EODs perform 11 × 11 grids Knight's tour scanning with microseconds response time, while the TAG lens drives sinusoidal axial scanning at 70 kHz. Together, these components enable rapid three-dimensional scanning over a confined volume of approximately 1 × 1 × 2 μm³. This compact scanning volume balances the need for precise particle localization and sufficient coverage of the surrounding cellular environment against the acquisition time and unnecessary illumination associated with larger imaging volumes (*44, 45*).

Langtaosha (LTS) Preprint doi: https://doi.org/10.65215/LTSpreprints.2026.11.24.000400. This version posted November 24, 2026. The copyright holder for this preprint (which was not certified by peer review) is the author/funder. Creative Commons license: CC Attribution-NonCommercial-NoDerivatives 4.0 https://creativecommons.org/licenses/by-nc-nd/4.0

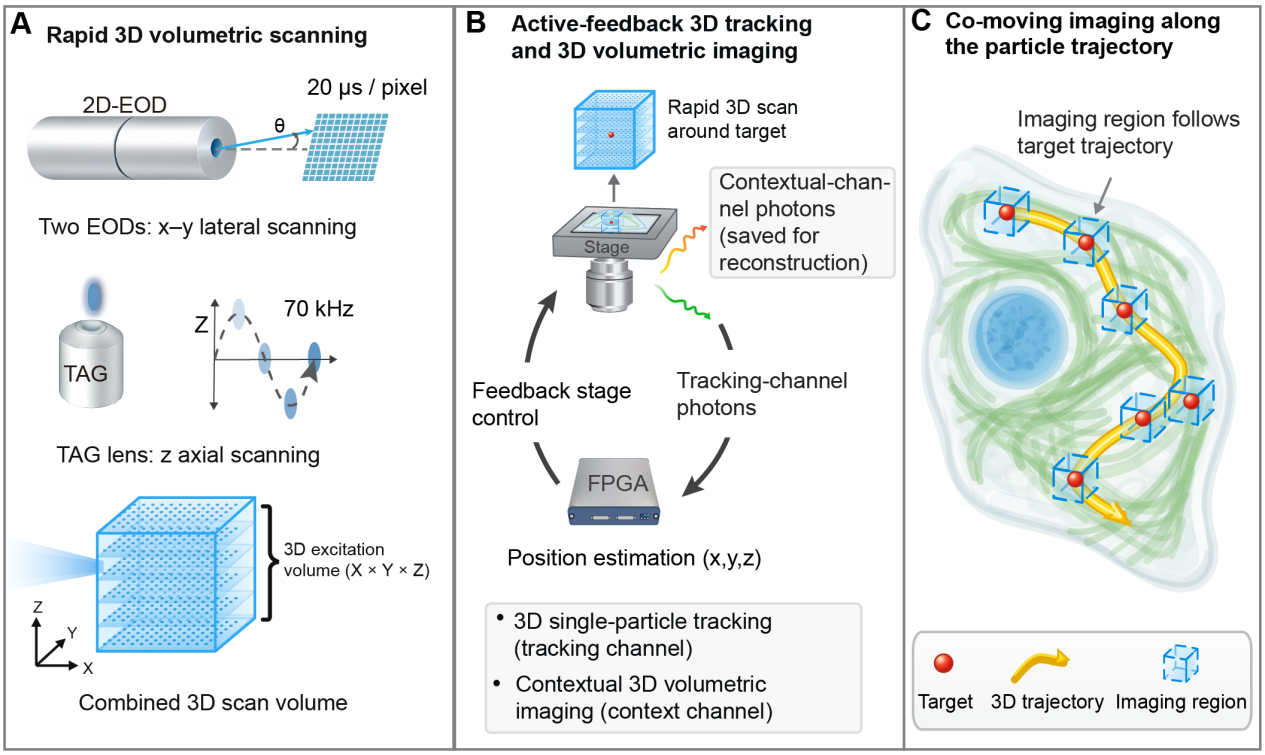


Figure 1. STARS acquisition principle. (**A**) A pair of EODs and a TAG lens provide rapid lateral and axial scanning. (**B**) Position estimates from tracking-channel photons drive piezoelectric feedback to keep the target near the local scan center, while the photons in the contextual channel are used to reconstruct the surrounding volume. (**C**) The sampled region follows the tracked particle in specimen coordinates, allowing contextual data to be registered along its trajectory and providing "street-view" volumetric imaging.

Photons detected in the tracking channel are detected by an avalanche photodiode (APD) and processed in real time by a field-programmable gate array (FPGA) to estimate target displacement from the scan center. The resulting position estimates drive piezoelectric feedback that translates the specimen and objective, maintaining the target near the center of the local scan while recording its three-dimensional trajectory (**Fig. 1B**). The local excitation volume therefore follows the particle in specimen coordinates as the target explores its environment.

In parallel, a separate detection channel records contextual fluorescence together with photon arrival times, lateral scan indices and TAG phases. These synchronized records assign detected photons to three-dimensional scan positions and enable offline reconstruction of the surrounding structures. Because the sinusoidal TAG scan produces unequal sampling times along the axial direction, photon counts in each axial layer are normalized by the corresponding laser

Langtaosha (LTS) Preprint doi: https://doi.org/10.65215/LTSpreprints.2026.11.24.000400. This version posted November 24, 2026. The copyright holder for this preprint (which was not certified by peer review) is the author/funder. Creative Commons license: CC Attribution-NonCommercial-NoDerivatives 4.0 https://creativecommons.org/licenses/by-nc-nd/4.0

dwell time (**fig. S2**). The reconstructed local volumes are then registered to the target trajectory, providing a three-dimensional record of the structures encountered by the moving particle in a common specimen coordinate system (**Fig. 1C**).

In this configuration, the contextual imaging region follows the target rather than remaining fixed, separating the size of the instantaneous sampling volume from the spatial extent of the trajectory. For an illustrative comparison, restricting acquisition to a $1 \times 1 \times 2$ μm^3 target-centered volume instead of a $10 \times 10 \times 10$ μm^3 fixed volume corresponds to a 500-fold reduction in sampled volume. This strategy confines acquisition to the target's immediate surroundings while feedback allows the sampled region to move through the specimen. The point-excitation, point-detection architecture supports target-locked acquisition over axial ranges of tens of micrometers, with the accessible range determined primarily by the travel of the piezoelectric feedback system. STARS thus combines compact local sampling with a trajectory-referenced view of structures distributed over a larger region.

Characterization of STARS performance

We first evaluated whether trajectory-guided sampling and reconstruction could preserve local three-dimensional structural information. Simulated volumes containing 200-nm fluorescent beads and microtubule-like structures were convolved with a point-spread function (PSF), sampled locally along freely diffusing or filament-directed trajectories, and reconstructed using the recorded trajectory coordinates. The resulting images preserved bead morphology and microtubule orientation and continuity within the sampled regions (**Fig. 2A,B** and **fig. S3**). We then compared STARS with piezoelectric-stage scanning in fixed specimens. Reconstructed microtubule networks retained the filament organization observed in the corresponding stage-scanned images (**Fig. 1C**). Argolight line, hollow-ring and cross patterns likewise showed consistent morphology between the two acquisition modes (**fig. S4**). Together, the simulated and experimental comparisons show that trajectory-referenced sampling preserves local structural features across different geometries.

Langtaosha (LTS) Preprint doi: https://doi.org/10.65215/LTSpreprints.2026.11.24.000400. This version posted November 24, 2026. The copyright holder for this preprint (which was not certified by peer review) is the author/funder. Creative Commons license: CC Attribution-NonCommercial-NoDerivatives 4.0 https://creativecommons.org/licenses/by-nc-nd/4.0

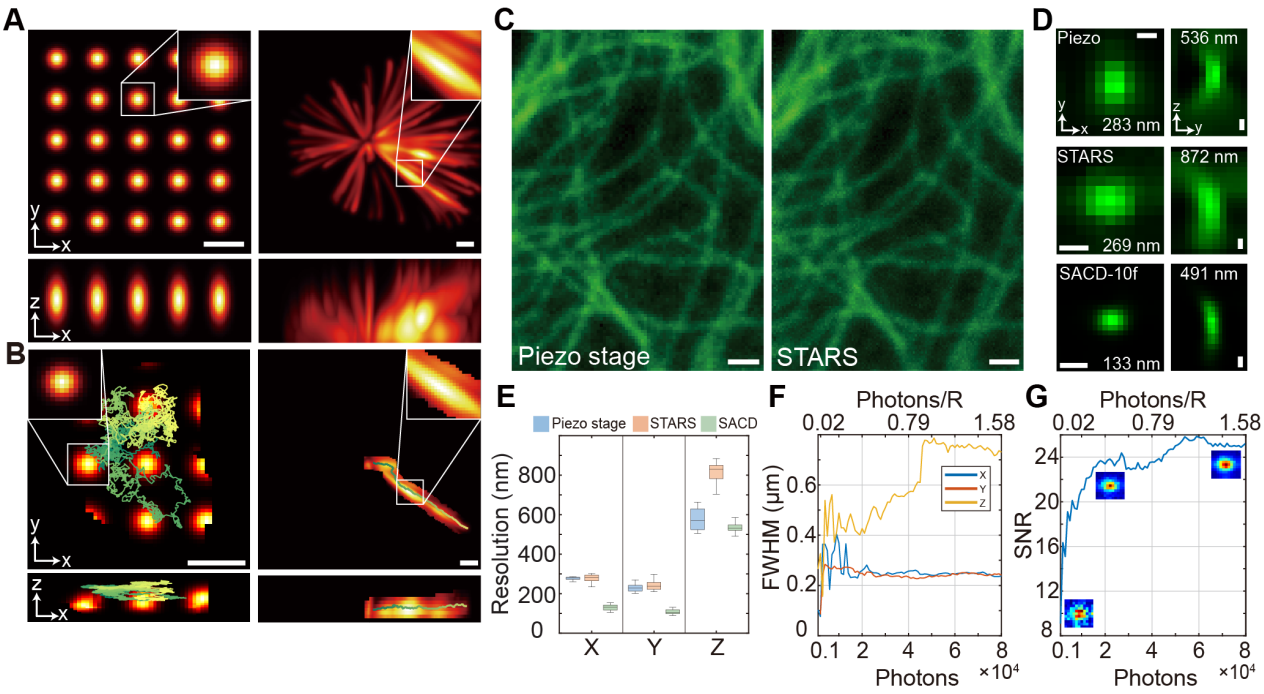


Figure 2. Contextual imaging performance of STARS. (**A**,**B**) Simulated PSF-convolved bead and microtubule volumes (**A**) and corresponding trajectory-referenced reconstructions (**B**). Scale bar: 1 μm. (**C**) Fixed-cell microtubules imaged by piezoelectric-stage scanning and STARS. Scale bar: 1 μm. (**D**) Representative bead images obtained by stage scanning, STARS and Sparse-SACD reconstruction from 10 frames. Scale bar: 200 nm. (**E**) FWHM values of bead images acquired by stage scanning and STARS, and after Sparse-SACD reconstruction. The FWHM values of stage scanning method: x, 276.70 ± 8.09 nm; y, 230.70 ± 21.32 nm; z, 575.30 ± 54.78 nm. The FWHM values of STARS: x, 279.65 ± 18.23 nm; y, 242.90 ± 25.52 nm; z, 815.20 ± 53.32 nm. The FWHM values of Sparse-SACD enhanced STARS: x, 129.10 ± 14.76 nm; y, 109.25 ± 16.88 nm; z, 535.15 ± 41.93 nm. Data are presented as mean ± standard deviation (SD), with n = 20 measurements. (**F**,**G**) FWHM (**F**) and SNR (**G**) as a function of accumulated detected photons; insets in (**G**) show representative bead reconstructions. Upper axes give equivalent integration times calculated as photons/R, where R is the detected photon count rate. The small FWHM of z axis in low photon count should be attributed to the low SNR.

We next quantified volumetric imaging performance using immobilized fluorescent microspheres, with spatial resolution characterized by the full width at half maximum (FWHM). STARS yielded lateral FWHM values of 279.65 ± 18.23 nm along x and 242.90 ± 25.52 nm along y, comparable to the corresponding stage-scanned values of 276.70 ± 8.09 nm and 230.70 ± 21.32

Langtaosha (LTS) Preprint doi: https://doi.org/10.65215/LTSpreprints.2026.11.24.000400. This version posted November 24, 2026. The copyright holder for this preprint (which was not certified by peer review) is the author/funder. Creative Commons license: CC Attribution-NonCommercial-NoDerivatives 4.0 https://creativecommons.org/licenses/by-nc-nd/4.0

nm. The axial FWHM was broader for STARS, at 815.20 ± 53.32 nm, compared with 575.30 ± 54.78 nm for stage scanning **(Fig. 1D,E)**. Spatial resolution could be further improved using Sparse-SACD, which combines fluorescence-fluctuation reconstruction with sparse deconvolution (*58*), producing a resolution of 129.10 ± 14.76 nm, 109.25 ± 16.88 nm and 535.15 ± 41.93 nm along x, y and z, respectively (**Fig. 1D,E and fig. S7-9**).

We next characterized the relationship between temporal sampling and volumetric image quality. A single volumetric scan requires 2.42 ms, corresponding to an 11 × 11 lateral scan with a dwell time of 20 μs per pixel and simultaneous axial scanning at 70 kHz. This scan period defines the minimum single-cycle volumetric sampling interval, whereas the practical temporal resolution depends on the integration time needed to collect sufficient photons for reliable reconstruction. Because photon arrival times are retained, the reconstruction window can be selected after acquisition, and photons from consecutive scan cycles can be combined to improve image quality.

To quantify this trade-off, we reconstructed fluorescent bead images using increasing numbers of detected photons and measured the resulting FWHM and signal-to-noise ratio (SNR). The lateral FWHM approached a plateau as photon number increased, whereas the axial FWHM remained more sensitive to photon statistics (**Fig. 1F**). The small axial FWHM values obtained at low photon counts were attributed to low SNR rather than improved axial resolution. SNR increased progressively with the accumulated photon count (**Fig. 1G**). These measurements establish a tunable trade-off between temporal sampling and photon-limited volumetric reconstruction quality. In parallel with volumetric acquisition, the tracking channel recorded particle coordinates at 1-ms intervals and nanometer-scale localization precision (**fig. S10**). STARS thus provides complementary readouts of a high-resolution three-dimensional particle trajectory and a target-centered volumetric image, with an integration time adaptable to the available contextual fluorescence signal.

Three-dimensional imaging of nanoparticle–membrane interactions.

We next applied STARS to relate nanoparticle dynamics to plasma membrane geometry in live U2OS cells. Individual 100-nm fluorescent microspheres were tracked while simultaneously imaging the surrounding CellMask Deep Red–labeled plasma membrane (**Fig. 3A–C**). In a representative trajectory, the particle initially diffused freely in the extracellular solution, exhibited a brief superdiffusive state as it approached the membrane, and became confined upon contact. It

Langtaosha (LTS) Preprint doi: https://doi.org/10.65215/LTSpreprints.2026.11.24.000400. This version posted November 24, 2026. The copyright holder for this preprint (which was not certified by peer review) is the author/funder. Creative Commons license: CC Attribution-NonCommercial-NoDerivatives 4.0 https://creativecommons.org/licenses/by-nc-nd/4.0

subsequently relocated to another membrane region during a second superdiffusive episode, followed by renewed confinement.

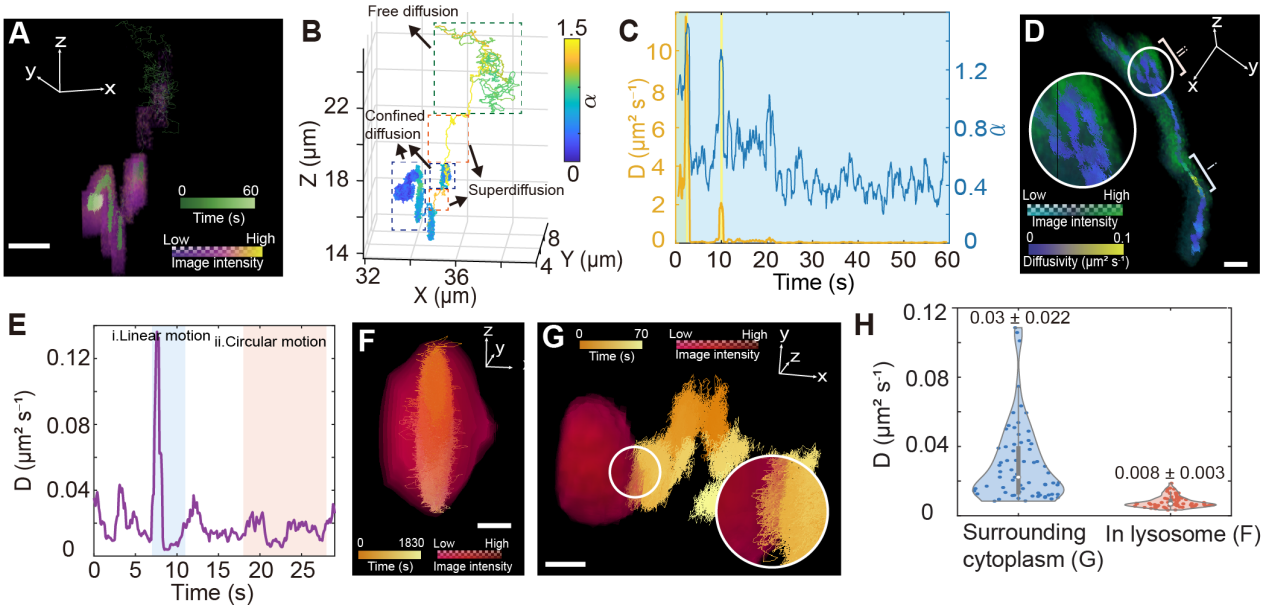


Figure 3. STARS resolves dynamic nanoparticle–organelle interactions in live cells. (**A**) A 100-nm fluorescent microsphere trajectory overlaid on a reconstructed CellMask Deep Red-labeled plasma membrane. Scale bar: 3 μm. (**B**) The 3D trajectory in (**A**), color-coded by the anomalous exponent α. The dashed boxes indicate trajectory segments exhibiting different diffusion modes. (**C**) Apparent diffusivity and anomalous exponent for the membrane-associated trajectory in (**A**), with shaded regions indicating distinct diffusion modes. (**D**) AgNP motion alongside microtubule structures labeled with SPY650-tubulin. The trajectory is color-coded by apparent diffusivity. Scale bar: 1 μm. (**E**) Apparent diffusivity extracted from the microtubule-associated trajectory shown in (**D**). Shaded regions indicate distinct motion regimes corresponding to linear and circular trajectories as marked in (**D**). (**F**,**G**) Representative AgNP trajectories overlaid on reconstructed LysoTracker-labeled lysosomes. The inset in (**G**) enlarges the circled region. Scale bar: 500 nm. (**H**) Apparent diffusion-coefficient distributions calculated from consecutive 1-s segments of the lysosome-related trajectories shown in (**F**) and (**G**). Each distribution contains 70 segments obtained from a single representative trajectory.

Time-resolved mean squared displacement (MSD) analysis revealed corresponding changes in apparent diffusivity and the anomalous diffusion exponent α, distinguishing the sequential motion states within the continuous trajectory **(Fig. 3B,C and fig. S11)**. Co-registration

Langtaosha (LTS) Preprint doi: https://doi.org/10.65215/LTSpreprints.2026.11.24.000400. This version posted November 24, 2026. The copyright holder for this preprint (which was not certified by peer review) is the author/funder. Creative Commons license: CC Attribution-NonCommercial-NoDerivatives 4.0 https://creativecommons.org/licenses/by-nc-nd/4.0

with the reconstructed membrane further showed that the final trajectory segment followed the local membrane topography, locating the confined motion relative to a three-dimensional surface **(Fig. 3A)**. This paired readout linked successive mobility states within the membrane geometry, allowing approach, confinement and relocation to be followed within one continuous three-dimensional recording.

Resolving nanoparticle dynamics near microtubules and lysosomes

We further examined nanoparticle dynamics in intracellular environments by tracking individual silver nanoparticles (AgNPs) while imaging nearby microtubules or lysosomes. For microtubule-associated measurements, the microtubule network was labeled with SPY650-tubulin. Co-registered volumetric images revealed AgNP motion spatially associated with microtubule filaments **(Fig. 3D)**. The trajectory contained approximately linear displacements and localized circular motion, accompanied by transitions between low- and high-mobility periods in the apparent diffusivity trajectory **(Fig. 3D,E)**. The simultaneous structural readout placed these heterogeneous motion patterns alongside the filament network, relating changes within a single particle trajectory to the local cytoskeletal organization.

To investigate nanoparticle–lysosome interactions, we tracked AgNPs while simultaneously imaging LysoTracker Deep Red–labeled lysosomes. One representative particle remained confined within a reconstructed lysosomal volume **(Fig. 3F)**, whereas another moved through the surrounding cytoplasmic region and transiently contacted a lysosome without sustained association **(Fig. 3G)**. Segment-wise analysis showed lower apparent diffusivity for the lysosome-associated particle than for the particle moving through the surrounding cytoplasmic region **(Fig. 3H)**. Together, these experiments demonstrate how STARS distinguishes filament-associated motion, confinement within a lysosome-associated volume and transient proximity to a lysosome within individual trajectories.

Multiparameter quantitative imaging of membrane protrusion dynamics

Finally, we used STARS to simultaneously quantify nanoparticle motion and the evolution of local membrane morphology during protrusion formation. TAT peptide-functionalized AgNPs (TATp-AgNPs) were tracked while the surrounding plasma membrane was imaged through the contextual fluorescence channel (**Fig. 4A** and **fig. S12**). In a 60-s trajectory segment, an AgNP exhibited

Langtaosha (LTS) Preprint doi: https://doi.org/10.65215/LTSpreprints.2026.11.24.000400. This version posted November 24, 2026. The copyright holder for this preprint (which was not certified by peer review) is the author/funder. Creative Commons license: CC Attribution-NonCommercial-NoDerivatives 4.0 https://creativecommons.org/licenses/by-nc-nd/4.0

confined motion around a developing membrane protrusion, showing a shell-like spatial distribution (**Fig. 4B–D** and **fig. S13A-D**). Orthogonal projections and three-dimensional rendering showed a close spatial association between the trajectory and the reconstructed protruding membrane **(Fig. 2B,C)**. A three-dimensional spherical fit yielded a characteristic trajectory diameter of approximately 1.66 μm **(fig. S13A)**.

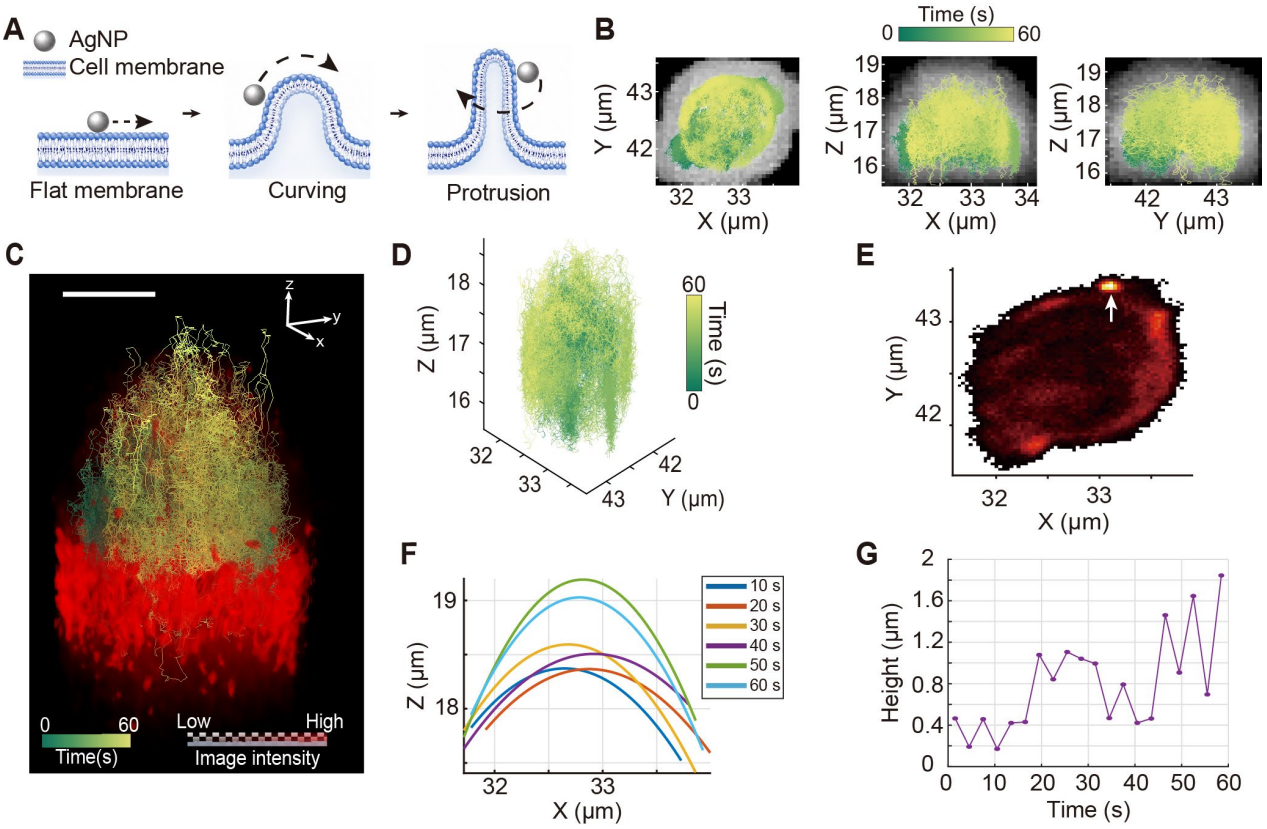


Figure 4. Simultaneous tracking of a nanoparticle and imaging of membrane protrusion growth. (**A**) Schematic of a TATp-AgNP near a developing membrane protrusion. (**B**) Orthogonal projections of the membrane reconstruction overlaid with the corresponding trajectory. (**C**) Three-dimensional rendering of the trajectory and reconstructed membrane. Scale bar: 1 μm. (**D**) Representative 60-s AgNP trajectory, colored by elapsed time. (**E**) Projected residence-time map showing nonuniform particle occupancy. (**F**) Membrane contours fitted to xz projections using consecutive, nonoverlapping 10-s windows. (**G**) Profile apex height relative to the baseline, obtained from profiles reconstructed at 3-s intervals.

Residence-time mapping revealed nonuniform particle occupancy around the protrusion, with distinct hotspots **(Fig. 4E and fig. S13C)**. Mean-squared displacement analysis and time-dependent mobility estimates were consistent with subdiffusive and confined motion **(fig.**

Langtaosha (LTS) Preprint doi: https://doi.org/10.65215/LTSpreprints.2026.11.24.000400. This version posted November 24, 2026. The copyright holder for this preprint (which was not certified by peer review) is the author/funder. Creative Commons license: CC Attribution-NonCommercial-NoDerivatives 4.0 https://creativecommons.org/licenses/by-nc-nd/4.0

S13B,E–G). The combined data therefore resolved spatially nonuniform exploration of the membrane-associated region over a prolonged trajectory.

We then quantified the temporal evolution of protrusion morphology from the contextual fluorescence data. Volumetric images were reconstructed using consecutive, nonoverlapping 10-s windows and projected onto the x–z plane. Membrane boundaries were extracted from these projections and fitted with second-order polynomials, revealing changes in the position and shape of the protrusion over time **(Fig. 4F and fig. S14)**. Membrane profiles reconstructed at 3-s intervals were subsequently used to quantify the protrusion apex height relative to the baseline. The height increased overall from approximately 0.4 μm to 1.8 μm within the analyzed 60-s interval **(Fig. 4G)**. The fitted profiles additionally yielded the curvature of the projected membrane contour, which varied over time and showed an overall increase during protrusion formation **(fig. S15)**. Together, these results demonstrate simultaneous quantification of nanoparticle occupancy, motion and local membrane remodeling, extending target-locked volumetric imaging from structural visualization to time-resolved analysis of a changing particle–membrane environment.

DISCUSSION

In summary, we developed STARS, which integrates active target locking with photon-resolved volumetric reconstruction to simultaneously capture high-precision three-dimensional trajectories and the evolving structural environment encountered along with them. The shared-scan architecture allows a small, interested acquisition volume to remain centered on the target as it explores a much larger region, avoiding repeated sampling of areas remote from immediate interaction. Moreover, photon-resolved recording further enables retrospective selection of the contextual integration window, allowing temporal resolution to be balanced against photon-limited reconstruction quality. The live-cell measurements demonstrate how this combined view relates heterogeneous nanoparticle dynamics to encounters with membranes, microtubules and lysosomes. The membrane protrusion experiments further show that the surrounding architecture can serve as a dynamic, quantitative readout rather than merely a structural reference. Together, these capabilities establish a target-centered framework for examining particle motion and local cellular remodeling within the same evolving three-dimensional interaction region.

Langtaosha (LTS) Preprint doi: https://doi.org/10.65215/LTSpreprints.2026.11.24.000400. This version posted November 24, 2026. The copyright holder for this preprint (which was not certified by peer review) is the author/funder. Creative Commons license: CC Attribution-NonCommercial-NoDerivatives 4.0 https://creativecommons.org/licenses/by-nc-nd/4.0

Although demonstrated here with single-color volumetric imaging, STARS is compatible with multicolor acquisition. Its single-photon detection architecture also provides a basis for future extension to volumetric fluorescence lifetime imaging, potentially linking particle dynamics to local physiological changes as well as structural remodeling (*59-61*). These extensions could broaden STARS from structural observation to functional interrogation of the environments encountered by moving particles. By shifting the reference frame of volumetric acquisition from the microscope stage to the moving target, STARS enables transient biological interactions to be examined within a co-moving three-dimensional context. This target-centered strategy extends volumetric microscopy beyond fixed-volume observation and provides a foundation for future adaptive and event-guided imaging, in which acquisition is directed toward evolving regions of biological interest (*62*).

MATERIALS AND METHODS

The Optical Setup of STARS

Three lasers with wavelengths of 488, 561, and 638 nm (LBX-488-60-CSB-PPA, LCX-561L-50-CSB-PPA, and LBX-638-100-CSB-PPA, OXXIUS) were used for excitation. Three pairs of achromatic doublet lenses and three pinholes were used to spatially filter the three laser beams. Two dichroic mirrors (T510lpxru and T588lpxr, Chroma) were used to combine the laser beams. The beam polarization was adjusted using a half-wave plate (AHWP05M-580, Thorlabs), and the beam was then passed through a Glan–Thompson polarizer (GLP10-A, LBTEK) before entering a pair of EODs (Model 310A, Conoptics Inc.). The laser beam was then expanded by a pair of lenses (AC254-075-A-ML and AC254-300-A-ML, Thorlabs). A tunable acoustic gradient lens (TAGLENS-T1, Mitutoyo) was used to modulate the axial focus position. Two relay lenses (AC254-250-A-ML and AC254-150-A-ML, Thorlabs) directed the beam to the objective lens (HC PL APO 100x/1.40OIL CS2, Leica). A dichroic mirror (ZT405/488/561/640 rpcv2, Chroma) was utilized for separating the excitation and emission light.

Subsequently, the collected light was separated by a dichroic mirror and guided to two APDs, which corresponding to the tracking and imaging APD channels. The band-pass filters were used to separate the excitation and fluorescence signal. The configuration of filters and dichroic mirror is described in **table S1.** For silver nanoparticle tracking, the depolarized scattering signal was detected, while a polarizer was used to suppress the scattering component with the same polarization as the excitation laser. **fig. S5** shows the workflow of the STARS system.

Langtaosha (LTS) Preprint doi: https://doi.org/10.65215/LTSpreprints.2026.11.24.000400. This version posted November 24, 2026. The copyright holder for this preprint (which was not certified by peer review) is the author/funder. Creative Commons license: CC Attribution-NonCommercial-NoDerivatives 4.0 https://creativecommons.org/licenses/by-nc-nd/4.0

Data acquisition was performed using LabVIEW (NI LabVIEW 2023). The 3D visualization of the multiresolution image was performed with Avizo Amira software (Avizo 3Dv2022.2).

EOD calibration

A 2D-electro optic deflector was calibrated using fluorescent beads immobilized on a coverslip. During calibration, the EODs were configured to perform an 11 × 11 Knight's Tour scanning pattern. To determine the physical spacing corresponding to each scan position, we established the relationship between the EOD input voltage and the lateral scan displacement (**fig. S6**).

A piezoelectric stage was used to scan fluorescent microspheres according to the following procedure. First, a single fluorescent bead was identified by translating the piezoelectric stage, and its fluorescence signal was detected by an avalanche photodiode (APD) to generate a reference image. Next, the EOD was activated to alternately scan between two discrete lateral positions. By applying different voltage offsets to the EODs, a series of bead images corresponding to distinct scan separations were recorded. Finally, the distance between the two bead images was extracted by fitting the intensity profiles, allowing the voltage-to-displacement conversion factor of the EODs to be determined.

TAG Axial Sampling

The TAG lens performs a sinusoidal axial scan, resulting in a non-uniform sampling density along the axial direction. The axial position is described by

$$z = A\sin(\phi + \phi_0) \tag{1}$$

where A is the oscillation amplitude, ϕ is the TAG phase, and ϕ_0 is the phase offset used for axial calibration.

The corresponding axial scanning velocity is

$$v_z = \frac{dz}{dt} = 2\pi f_{TAG} A\cos(\phi + \phi_0) \tag{2}$$

where f_{TAG} is the TAG oscillation frequency.

Because the scanning velocity approaches zero near the turning points of the sinusoidal trajectory, the excitation volume remains longer in these axial regions. Consequently, a uniform fluorescent sample would generate a non-uniform photon distribution, with increased photon counts near the axial extremes. This effect originates from unequal sampling time rather than true variations in fluorophore density.

Langtaosha (LTS) Preprint doi: https://doi.org/10.65215/LTSpreprints.2026.11.24.000400. This version posted November 24, 2026. The copyright holder for this preprint (which was not certified by peer review) is the author/funder. Creative Commons license: CC Attribution-NonCommercial-NoDerivatives 4.0 https://creativecommons.org/licenses/by-nc-nd/4.0

To compensate for this bias, the axial range is divided into N_z discrete layers. For each layer i, the effective TAG dwell time is calculated from the corresponding phase interval:

$$\Delta t_i = 2\frac{\Delta\phi_i}{2\pi f_{TAG}} \tag{3}$$

where $\Delta\phi_i$ denotes the phase interval corresponding to a single monotonic scan branch. The factor of 2 accounts for the upward and downward passages through the same axial layer during each TAG cycle.

The measured photon counts are then normalized by the dwell time:

$$I_i^{corr} = \frac{I_i}{\Delta t_i} \tag{4}$$

This correction removes the intensity accumulation caused by the non-uniform axial scanning speed of the TAG lens and produces a more uniform representation of the fluorophore distribution throughout the reconstructed volume.

Live-cell labelling of lysosomes and tubulin and single-particle tracking of AgNPs

Lysosomes and microtubules were labeled separately in different U-2 OS cell samples. For lysosomal labelling, LysoTracker Deep Red (Invitrogen, catalogue no. L12492) was diluted in prewarmed complete growth medium to a final concentration of 50 nM. When the cells reached the desired confluence, the culture medium was replaced with the probe-containing medium, and the cells were incubated for 2 h at 37 °C under standard growth conditions. The labelling solution was subsequently replaced with prewarmed FluoroBrite DMEM before AgNP treatment and imaging.

For live-cell microtubule labelling, SPY650-tubulin (Spirochrome, catalogue no. SC503) was reconstituted in anhydrous dimethyl sulfoxide to prepare a 1000× stock solution. Immediately before staining, SPY650-tubulin was diluted 1:1000 to a final concentration of 1× in freshly prepared complete growth medium supplemented with verapamil at a final concentration of 1 μM. When the cells reached the desired density, the culture medium was replaced with the freshly prepared staining solution, ensuring that all cells were completely covered. The cells were incubated for 1 h at 37 °C in a humidified atmosphere containing 5% CO_2. The staining solution was subsequently replaced with prewarmed FluoroBrite DMEM before AgNP treatment and imaging.

Langtaosha (LTS) Preprint doi: https://doi.org/10.65215/LTSpreprints.2026.11.24.000400. This version posted November 24, 2026. The copyright holder for this preprint (which was not certified by peer review) is the author/funder. Creative Commons license: CC Attribution-NonCommercial-NoDerivatives 4.0 https://creativecommons.org/licenses/by-nc-nd/4.0

The lysosome- and tubulin-labeled cell samples were subjected to identical AgNP treatment and tracking procedures. Immediately before single-particle tracking, silver nanoparticles (AgNPs) were diluted in FluoroBrite™ DMEM and added to the cells at a final concentration of 10 μg/ml. Cells were incubated with AgNPs for 30 min at 37 °C, after which real-time single-particle tracking was initiated immediately.

Three-dimensional tracking of fluorescent microspheres above the cell surface

U-2 OS cells were seeded at a density of 15,000 cells per glass-bottom imaging dish (NEST Biotechnology, catalogue no. 801001, China) and cultured for 18–20 h at 37 °C in a humidified atmosphere containing 5% CO_2 until they reached approximately 60–80% confluence. For plasma membrane labelling, live cells were incubated with a freshly prepared 1× working solution of CellMask Plasma Membrane Stain (Invitrogen, catalogue no. C10046) in prewarmed FluoroBrite™ DMEM for 10 min at 37 °C. The staining solution was subsequently removed and replaced with fresh FluoroBrite™ DMEM.

Dragon Green fluorescent carboxylated polystyrene microspheres with a nominal diameter of 100 nm (Bangs Laboratories, catalogue no. FCDG002) were diluted 1:10,000 in FluoroBrite™ DMEM and added directly to the cells. After identifying the focal plane of the cells, the tracking plane was manually positioned approximately 25 μm above the cell focal plane, within the extracellular medium. Real-time three-dimensional single-particle tracking was then initiated.

Immunofluorescence staining of tubulin

U-2OS cells were maintained in McCoy's 5A medium (Pricella, PM150715, China) supplemented with 10% fetal bovine serum and 1% penicillin–streptomycin at 37 °C in a humidified incubator containing 5% CO_2. For immunofluorescence staining, cells were seeded onto sterile glass coverslips in 6-well plates and cultured to approximately 60–70% confluence before the indicated treatments.

Cells were washed three times with phosphate-buffered saline (PBS) and fixed with pre-chilled methanol at −20 °C for 10 min. After fixation, cells were washed three times with PBS and blocked with 5% bovine serum albumin (BSA) in PBS for 1 h at room temperature. Cells were subsequently incubated overnight at 4 °C with an alpha Tubulin Monoclonal Antibody (B-5-1-2) (Invitrogen™ ;32-2500) diluted 1:200 in PBS containing 1% bovine serum albumin. After three washes with PBS, cells were incubated with a goat anti-mouse IgG–Atto 488 secondary antibody (Sigma-Aldrich, catalogue no. 62197) diluted 1:400 for 1 h at room temperature in the dark. Coverslips

Langtaosha (LTS) Preprint doi: https://doi.org/10.65215/LTSpreprints.2026.11.24.000400. This version posted November 24, 2026. The copyright holder for this preprint (which was not certified by peer review) is the author/funder. Creative Commons license: CC Attribution-NonCommercial-NoDerivatives 4.0 https://creativecommons.org/licenses/by-nc-nd/4.0

were washed three times with PBS and mounted onto glass slides using ProLong™ Glass Antifade Mountant (Invitrogen™, P36982).

Functionalization of silver nanoparticles and live-cell tracking

Silver nanoparticles (AgNPs) were functionalized with the TAT peptide (TATp) according to a previously described method(*63*). Briefly, streptavidin was thiolated using NHS-PEG-Thiol to facilitate its attachment to the AgNP surface, followed by conjugation of biotinylated TATp to the streptavidin-functionalized AgNPs. The resulting TATp-functionalized AgNPs (TATp-AgNPs) were stored at 4 °C and used within 7 days of preparation.

For live-cell tracking experiments, U-2OS cells were seeded in glass-bottom culture dishes (Nest; 801001, China) at a seeding density of 15,000 cells per dish, and incubated for 18-20 h at 37 °C in 5% CO2 in order to allow the cells to reach 60∼80% confluence. Immediately before tracking, the cells were incubated with CellMask™ Plasma Membrane Stains to fluorescently label the plasma membrane. The cells were subsequently maintained in FluoroBrite™ DMEM throughout the experiment. Immediately before tracking, TATp–AgNPs or unmodified AgNPs were added to a final particle concentration of approximately 3 pM.

Mean squared displacement and anomalous diffusion analysis

Three-dimensional particle trajectories were analyzed to characterize the temporal evolution of particle motion. The trajectory coordinates were sampled at 1-ms intervals. For a trajectory segment **r**(t) = [x(t), y(t), z(t)], the mean squared displacement (MSD) was calculated as

$$MSD(\tau) = \langle |r(t+\tau) - r(t)|^2 \rangle \tag{5}$$

where τ is the lag time.

To characterize time-dependent diffusion behavior, MSD analysis was performed using a sliding window of 1 s with a step size of 0.1 s. Within each window, the MSD was calculated for lag times up to one-quarter of the window duration. The first one-third of the resulting lag-time points was used for nonlinear least-squares fitting to the anomalous diffusion model

$$MSD(\tau) = 6D_\alpha \tau^\alpha \tag{6}$$

Where D_α is the apparent diffusion and α is the anomalous diffusion exponent.

Sphere fitting for trajectory diameter estimation

To estimate the diameter of the membrane bleb, the trajectory was fitted to a sphere by nonlinear least-squares minimization of the radial residuals.. Let (x_i, y_i, z_i) denote the coordinates of the i

Langtaosha (LTS) Preprint doi: https://doi.org/10.65215/LTSpreprints.2026.11.24.000400. This version posted November 24, 2026. The copyright holder for this preprint (which was not certified by peer review) is the author/funder. Creative Commons license: CC Attribution-NonCommercial-NoDerivatives 4.0 https://creativecommons.org/licenses/by-nc-nd/4.0

th localization. Assuming that the trajectory lies on a spherical surface with center (x_c, y_c, z_c) and radius R, the sphere satisfies:

$$(x-x_c)^2+(y-y_c)^2+(z-z_c)^2=R^2 \tag{7}$$

For each localization, the Euclidean distance to the sphere center was calculated as

$$r_i=\sqrt{(x_i-x_c)^2+(y_i-y_c)^2+(z_i-z_c)^2} \tag{8}$$

The fitting residual was defined as the radial deviation from the spherical surface

$$\mathrm{e}_i=r_i-R \tag{9}$$

and the optimal sphere parameters were obtained by minimizing the sum of squared residuals

$$\min_{x_c,y_c,z_c,R}\sum_{i=1}^{N}(r_i-R)^2 \tag{10}$$

The initial sphere center was set to the centroid of all localization coordinates, and the initial radius was defined as the mean distance from the centroid to the trajectory points. The fitted sphere radius was used to calculate the membrane bleb diameter as

$$Diameter=2R \tag{11}$$

Membrane curvature calculation

The membrane boundary was first extracted from the fluorescence intensity profile and converted from pixel coordinates to physical coordinates using the calibrated pixel sizes. To obtain a smooth representation of the membrane profile, the extracted boundary was fitted using a second-order polynomial:

$$\mathrm{z}(x)=ax^2+bx+c \tag{12}$$

where *x* and *z* represent the lateral and axial coordinates of the membrane boundary, respectively, and *a,b* and *c* are the fitting coefficients.

The first derivative of the fitted profile is

$$\mathrm{z}'(x)=2ax+b \tag{13}$$

and the second derivative is

$$\mathrm{z}''(\mathrm{x})=2\mathrm{a} \tag{14}$$

The local curvature of the membrane was calculated as

$$\kappa(\mathrm{x})=\frac{|\,\mathrm{z}''(\mathrm{x})\,|}{[1+\mathrm{z}'(\mathrm{x})^2]^{\frac{3}{2}}} \tag{15}$$

Langtaosha (LTS) Preprint doi: https://doi.org/10.65215/LTSpreprints.2026.11.24.000400. This version posted November 24, 2026. The copyright holder for this preprint (which was not certified by peer review) is the author/funder. Creative Commons license: CC Attribution-NonCommercial-NoDerivatives 4.0 https://creativecommons.org/licenses/by-nc-nd/4.0

Substituting the first- and second-order derivatives of the quadratic function gives

$$\kappa(x) = \frac{2|a|}{[1+(2ax+b)^2]^{\frac{3}{2}}} \tag{16}$$

where $\kappa(x)$ is the local membrane curvature.

REFERENCES

1. Gao, Z., Li, Q., Fan, C. & Hou, S. Deciphering live-cell biomolecular dynamics with single-molecule fluorescence imaging. *Science Bulletin* **69**, 1823-1828 (2024).
2. Zhao, Y. et al. Isotropic super-resolution light-sheet microscopy of dynamic intracellular structures at subsecond timescales. *Nature Methods* **19**, 359-369 (2022).
3. Chen, B.-C. et al. Lattice light-sheet microscopy: Imaging molecules to embryos at high spatiotemporal resolution. *Science* **346**, 1257998 (2014).
4. Ouyang, Z. et al. Elucidating subcellular architecture and dynamics at isotropic 100-nm resolution with 4Pi-SIM. *Nature Methods* **22**, 335-347 (2025).
5. Simon, F., Weiss, L.E. & van Teeffelen, S. A guide to single-particle tracking. *Nature Reviews Methods Primers* **4**, 66 (2024).
6. Calebiro, D. & Koszegi, Z. The subcellular dynamics of GPCR signaling. *Molecular and Cellular Endocrinology* **483**, 24-30 (2019).
7. Reck-Peterson, S.L., Redwine, W.B., Vale, R.D. & Carter, A.P. The cytoplasmic dynein transport machinery and its many cargoes. *Nature Reviews Molecular Cell Biology* **19**, 382-398 (2018).
8. Brandenburg, B. & Zhuang, X. Virus trafficking – learning from single-virus tracking. *Nature Reviews Microbiology* **5**, 197-208 (2007).
9. Gilleron, J. et al. Image-based analysis of lipid nanoparticle–mediated siRNA delivery, intracellular trafficking and endosomal escape. *Nature Biotechnology* **31**, 638-646 (2013).
10. Johnson, C., Exell, J., Lin, Y., Aguilar, J. & Welsher, K.D. Capturing the start point of the virus–cell interaction with high-speed 3D single-virus tracking. *Nature Methods* **19**, 1642-1652 (2022).
11. Monnier, N. et al. Inferring transient particle transport dynamics in live cells. *Nature Methods* **12**, 838-840 (2015).
12. Liao, Y.-C. et al. RNA Granules Hitchhike on Lysosomes for Long-Distance Transport, Using Annexin A11 as a Molecular Tether. *Cell* **179**, 147-164.e120 (2019).
13. Lee, J.E., Cathey, P.I., Wu, H., Parker, R. & Voeltz, G.K. Endoplasmic reticulum contact sites regulate the dynamics of membraneless organelles. *Science* **367**, eaay7108 (2020).
14. van Heerden, B., Vickers, N.A., Krüger, T.P.J. & Andersson, S.B. Real-Time Feedback-Driven Single-Particle Tracking: A Survey and Perspective. *Small* **18**, 2107024 (2022).

Langtaosha (LTS) Preprint doi: https://doi.org/10.65215/LTSpreprints.2026.11.24.000400. This version posted November 24, 2026. The copyright holder for this preprint (which was not certified by peer review) is the author/funder. Creative Commons license: CC Attribution-NonCommercial-NoDerivatives 4.0 https://creativecommons.org/licenses/by-nc-nd/4.0

15. Dean, K.M. et al. Imaging subcellular dynamics with fast and light-efficient volumetrically parallelized microscopy. *Optica* **4**, 263-271 (2017).
16. Wu, Y. et al. Spatially isotropic four-dimensional imaging with dual-view plane illumination microscopy. *Nature Biotechnology* **31**, 1032-1038 (2013).
17. Voleti, V. et al. Real-time volumetric microscopy of in vivo dynamics and large-scale samples with SCAPE 2.0. *Nature Methods* **16**, 1054-1062 (2019).
18. Wagner, N. et al. Instantaneous isotropic volumetric imaging of fast biological processes. *Nature Methods* **16**, 497-500 (2019).
19. Hua, X., Liu, W. & Jia, S. High-resolution Fourier light-field microscopy for volumetric multi-color live-cell imaging. *Optica* **8**, 614-620 (2021).
20. Wang, Z. et al. Real-time volumetric reconstruction of biological dynamics with light-field microscopy and deep learning. *Nature Methods* **18**, 551-556 (2021).
21. Wu, Y. et al. Multiview confocal super-resolution microscopy. *Nature* **600**, 279-284 (2021).
22. Liang, Q. et al. High-fidelity tissue super-resolution imaging achieved with confocal2 spinning-disk image scanning microscopy. *Light: Science & Applications* **14**, 260 (2025).
23. Wang, Z. et al. Kilohertz volumetric imaging of in vivo dynamics using squeezed light field microscopy. *Nature Methods* **22**, 2194-2204 (2025).
24. Xiao, S. et al. High-contrast multifocus microscopy with a single camera and z-splitter prism. *Optica* **7**, 1477-1486 (2020).
25. Hirata Miyasaki, E. et al. High-speed 3D imaging with a 25-camera multifocus microscope. *Optica* **12**, 1230-1241 (2025).
26. Dibaji, H. et al. Axial de-scanning using remote focusing in the detection arm of light-sheet microscopy. *Nature Communications* **15**, 5019 (2024).
27. Silvestri, L. et al. Universal autofocus for quantitative volumetric microscopy of whole mouse brains. *Nature Methods* **18**, 953-958 (2021).
28. Zhu, L. et al. Adaptive-learning physics-assisted light-field microscopy enables day-long and millisecond-scale super-resolution imaging of 3D subcellular dynamics. *Nature Communications* **16**, 7132 (2025).
29. Lu, Z. et al. Virtual-scanning light-field microscopy for robust snapshot high-resolution volumetric imaging. *Nature Methods* **20**, 735-746 (2023).
30. Badon, A. et al. Video-rate large-scale imaging with Multi-Z confocal microscopy. *Optica* **6**, 389-395 (2019).
31. Abrahamsson, S. et al. Fast multicolor 3D imaging using aberration-corrected multifocus microscopy. *Nature Methods* **10**, 60-63 (2013).
32. Böhm, U.L. & Judkewitz, B. Fast and light-efficient remote focusing for volumetric voltage imaging. *Nature Communications* **15**, 9555 (2024).
33. Li, H. et al. Three-dimensional random-access confocal microscopy with 3D remote focusing system. *Communications Engineering* **3**, 166 (2024).
34. Hoebe, R.A. et al. Controlled light-exposure microscopy reduces photobleaching and phototoxicity in fluorescence live-cell imaging. *Nature Biotechnology* **25**, 249-253 (2007).

Langtaosha (LTS) Preprint doi: https://doi.org/10.65215/LTSpreprints.2026.11.24.000400. This version posted November 24, 2026. The copyright holder for this preprint (which was not certified by peer review) is the author/funder. Creative Commons license: CC Attribution-NonCommercial-NoDerivatives 4.0 https://creativecommons.org/licenses/by-nc-nd/4.0

35. Dreier, J. et al. Smart scanning for low-illumination and fast RESOLFT nanoscopy in vivo. *Nature Communications* **10**, 556 (2019).
36. Li, B., Wu, C., Wang, M., Charan, K. & Xu, C. An adaptive excitation source for high-speed multiphoton microscopy. *Nature Methods* **17**, 163-166 (2020).
37. Xiao, S. et al. Large-scale deep tissue voltage imaging with targeted-illumination confocal microscopy. *Nature Methods* **21**, 1094-1102 (2024).
38. Stepp, W.L. et al. Smart hybrid microscopy for cell-friendly detection of rare events. *Nature Communications* **17**, 1423 (2026).
39. Abouakil, F. et al. An adaptive microscope for the imaging of biological surfaces. *Light: Science & Applications* **10**, 210 (2021).
40. Mahecic, D. et al. Event-driven acquisition for content-enriched microscopy. *Nature Methods* **19**, 1262-1267 (2022).
41. Alvelid, J., Damenti, M., Sgattoni, C. & Testa, I. Event-triggered STED imaging. *Nature Methods* **19**, 1268-1275 (2022).
42. Alvelid, J., Koerfer, A. & Eggeling, C. Smart event-triggered MINFLUX microscopy to catch and follow rare events. *Nature Communications* **17**, 4558 (2026).
43. Berrevoets, E.S. et al. Smart 3D super-resolution microscopy reveals the architecture of the RNA scaffold in a nuclear body. *Nature Communications* **16**, 10689 (2025).
44. Hou, S., Lang, X. & Welsher, K. Robust real-time 3D single-particle tracking using a dynamically moving laser spot. *Opt. Lett.* **42**, 2390-2393 (2017).
45. Hou, S., Exell, J. & Welsher, K. Real-time 3D single molecule tracking. *Nature Communications* **11**, 3607 (2020).
46. Hou, S., Zhang, C., Niver, A. & Welsher, K. Mapping nanoscale forces and potentials in live cells with microsecond 3D single-particle tracking. *bioRxiv*, 2022.2006.2027.497788 (2022).
47. Germann, J.A. & Davis, L.M. Three-dimensional tracking of a single fluorescent nanoparticle using four-focus excitation in a confocal microscope. *Opt. Express* **22**, 5641-5650 (2014).
48. Perillo, E.P. et al. Deep and high-resolution three-dimensional tracking of single particles using nonlinear and multiplexed illumination. *Nature Communications* **6**, 7874 (2015).
49. Cang, H., Wong, C.M., Xu, C.S., Rizvi, A.H. & Yang, H. Confocal three dimensional tracking of a single nanoparticle with concurrent spectroscopic readouts. *Appl Phys Lett* **88**, 3 (2006).
50. Lessard, G.A., Goodwin, P.M. & Werner, J.H. Three-dimensional tracking of individual quantum dots. *Appl Phys Lett* **91**, 3 (2007).
51. Katayama, Y. et al. Real-time nanomicroscopy via three-dimensional single-particle tracking. *ChemPhysChem* **10**, 2458-2464 (2009).
52. Levi, V., Ruan, Q., Kis-Petikova, K. & Gratton, E. Scanning FCS, a novel method for three-dimensional particle tracking. *Biochem. Soc. Trans.* **31**, 997-1000 (2003).
53. McHale, K., Berglund, A.J. & Mabuchi, H. Quantum dot photon statistics measured by three-dimensional particle tracking. *Nano Lett.* **7**, 3535-3539 (2007).

Langtaosha (LTS) Preprint doi: https://doi.org/10.65215/LTSpreprints.2026.11.24.000400. This version posted November 24, 2026. The copyright holder for this preprint (which was not certified by peer review) is the author/funder. Creative Commons license: CC Attribution-NonCommercial-NoDerivatives 4.0 https://creativecommons.org/licenses/by-nc-nd/4.0

54. Amselem, E., Broadwater, B., Havermark, T., Johansson, M. & Elf, J. Real-time single-molecule 3D tracking in E. coli based on cross-entropy minimization. *Nature Communications* **14**, 1336 (2023).
55. Ashley, T.T., Gan, E.L., Pan, J. & Andersson, S.B. Tracking single fluorescent particles in three dimensions via extremum seeking. *Biomedical Optics Express* **7**, 3355-3376 (2016).
56. Bucci, A. et al. 4D Single-particle tracking with asynchronous read-out single-photon avalanche diode array detector. *Nature Communications* **15**, 6188 (2024).
57. Hou, S. & Welsher, K. An Adaptive Real-Time 3D Single Particle Tracking Method for Monitoring Viral First Contacts. *Small* **15**, e1903039 (2019).
58. Zhao, W. et al. Enhanced detection of fluorescence fluctuations for high-throughput super-resolution imaging. *Nature Photonics* **17**, 806-813 (2023).
59. Ma, Y. et al. Light-field tomographic fluorescence lifetime imaging microscopy. *Proceedings of the National Academy of Sciences* **121**, e2402556121 (2024).
60. Torrado, B., Pannunzio, B., Malacrida, L. & Digman, M.A. Fluorescence lifetime imaging microscopy. *Nature Reviews Methods Primers* **4**, 80 (2024).
61. Dunsing-Eichenauer, V. et al. Fast volumetric fluorescence lifetime imaging of multicellular systems using single-objective light-sheet microscopy. *Communications Biology* **8**, 1785 (2025).
62. Rates, A., Passmore, J.B., Norlin, N. & Kapitein, L.C. Smart microscopy: adaptive microscope control to improve the way we see life. *npj Imaging* **4**, 14 (2026).
63. Hou, S., Zhang, C., Niver, A. & Welsher, K.D. Mapping Nanoscale Forces and Potentials in Live Cells with Microsecond 3D Single-Particle Tracking. *Chemical & Biomedical Imaging* (2026).

Acknowledgments

Funding: This work was supported by the Major Program of Shenzhen Bay Laboratory (grant no. C1012524004), the National Natural Science Foundation of China (grant no. 22574109), the Scientific Research Innovation Capability Support Project for Young Faculty (ZYGXQNJSKYCXNLZCXM-H7), and the startup funding from Shenzhen Bay Laboratory.

Authors contributions: S. H. conceived and supervised the project. Z.D. and Y. W. performed experiments and data analysis. Y. L. performed data analysis. H. S., Y. H. and H. L. discussed the results. Z. D. and S. H. wrote the manuscript. All authors reviewed and approved the manuscript.

Competing interest: The authors declare that they have no competing interests.

Data, code, and materials availability: The data that support the findings of this study are available from the corresponding author upon reasonable request.

Langtaosha (LTS) Preprint doi: https://doi.org/10.65215/LTSpreprints.2026.11.24.000400. This version posted November 24, 2026. The copyright holder for this preprint (which was not certified by peer review) is the author/funder. Creative Commons license: CC Attribution-NonCommercial-NoDerivatives 4.0 https://creativecommons.org/licenses/by-nc-nd/4.0

625

626

Langtaosha (LTS) Preprint doi: https://doi.org/10.65215/LTSpreprints.2026.11.24.000400. This version posted November 24, 2026. The copyright holder for this preprint (which was not certified by peer review) is the author/funder. Creative Commons license: CC Attribution-NonCommercial-NoDerivatives 4.0 https://creativecommons.org/licenses/by-nc-nd/4.0

Supplementary Materials for

Target-locked volumetric microscopy

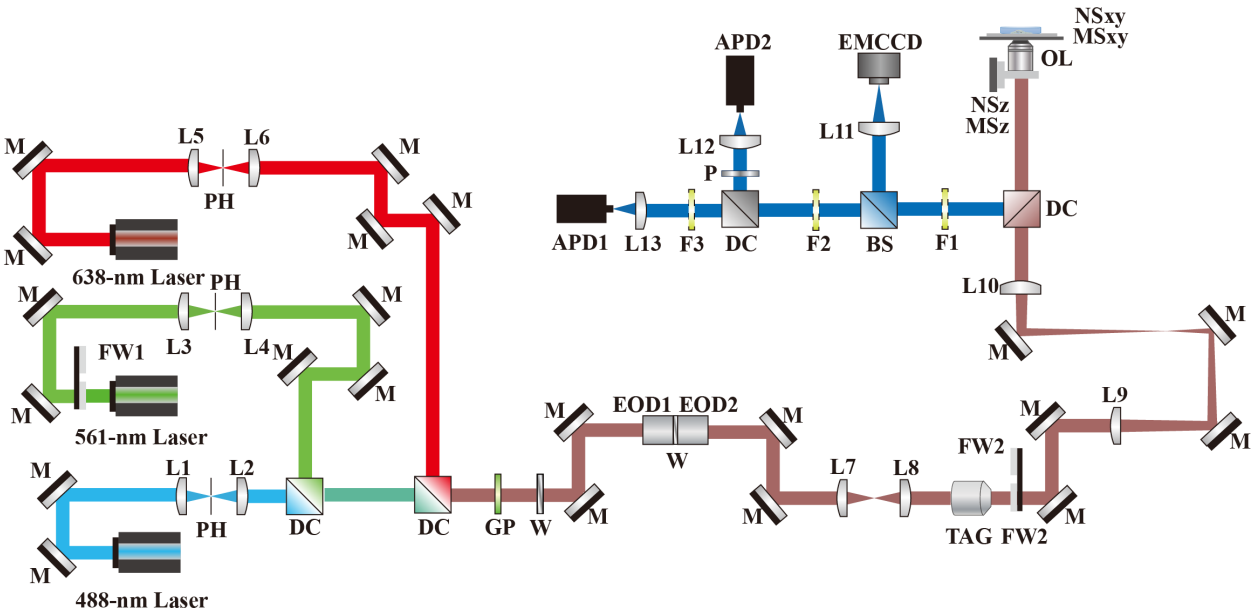
ZiChen Ding *et al.*

Corresponding author: Shangguo Hou, shangguo.hou@szbl.ac.cn

This PDF file includes:

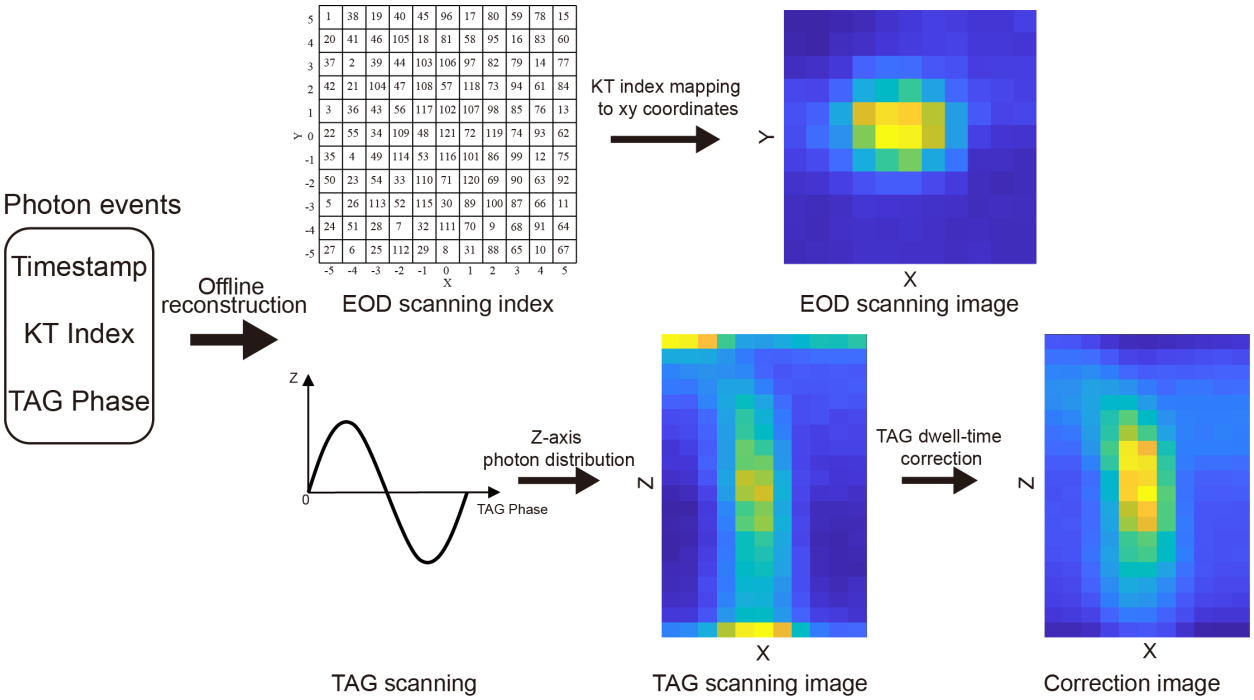
Figs. S1 to S15
Tables S1

Langtaosha (LTS) Preprint doi: https://doi.org/10.65215/LTSpreprints.2026.11.24.000400. This version posted November 24, 2026. The copyright holder for this preprint (which was not certified by peer review) is the author/funder. Creative Commons license: CC Attribution-NonCommercial-NoDerivatives 4.0 https://creativecommons.org/licenses/by-nc-nd/4.0



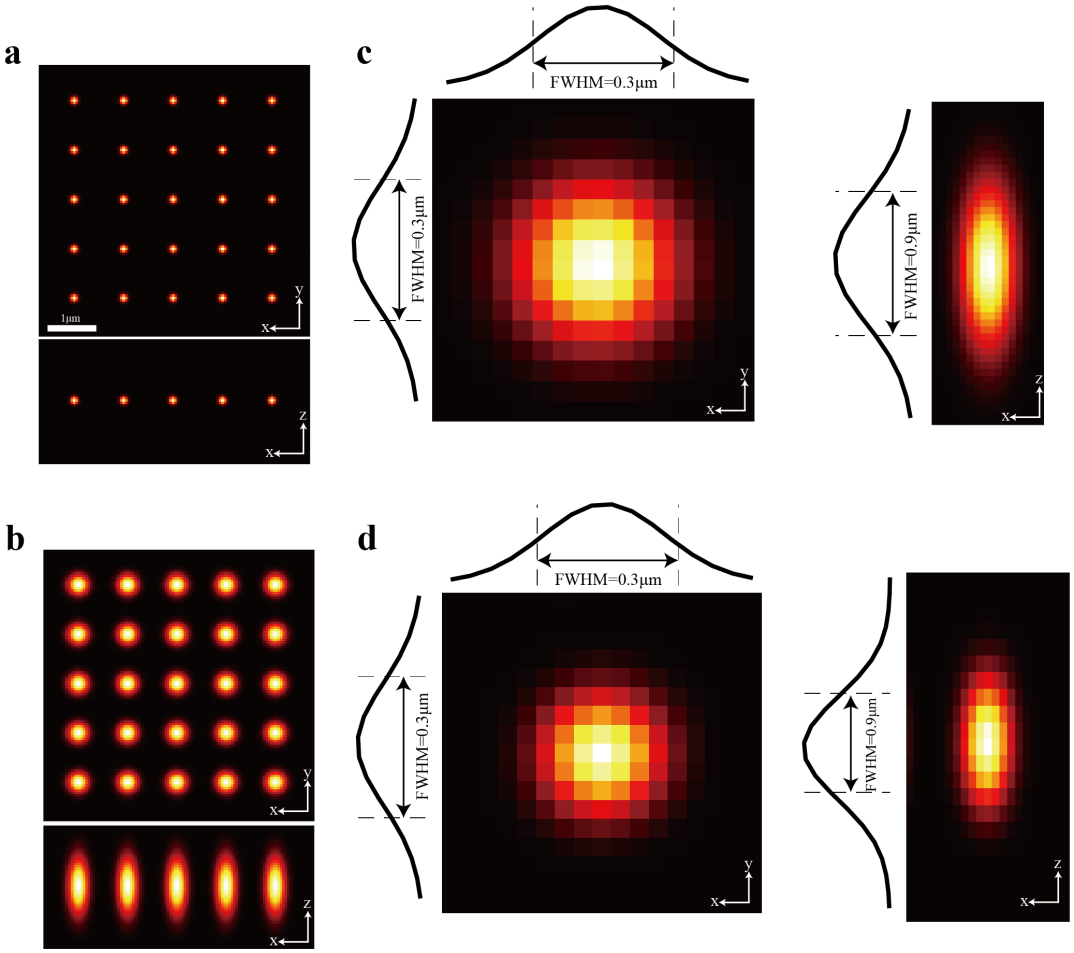
Supplementary Figure 1. Optical layout of STARS. M, mirror; L, lens; PH, pinhole; FW, filter wheel; DC, dichroic mirror; GP, Glan–Thompson polarizer; W, half-wave plate; EOD, electro-optic deflector; TAG, tunable acoustic gradient lens; OL, objective lens; MSxy and MSz, lateral and axial micropositioning stages; NSxy and NSz, lateral and axial nanopositioning stages; P, polarizer; F, fluorescence filter; BS, beam splitter; APD, avalanche photodiode; EMCCD, electron-multiplying charge-coupled device.

Langtaosha (LTS) Preprint doi: https://doi.org/10.65215/LTSpreprints.2026.11.24.000400. This version posted November 24, 2026. The copyright holder for this preprint (which was not certified by peer review) is the author/funder. Creative Commons license: CC Attribution-NonCommercial-NoDerivatives 4.0 https://creativecommons.org/licenses/by-nc-nd/4.0



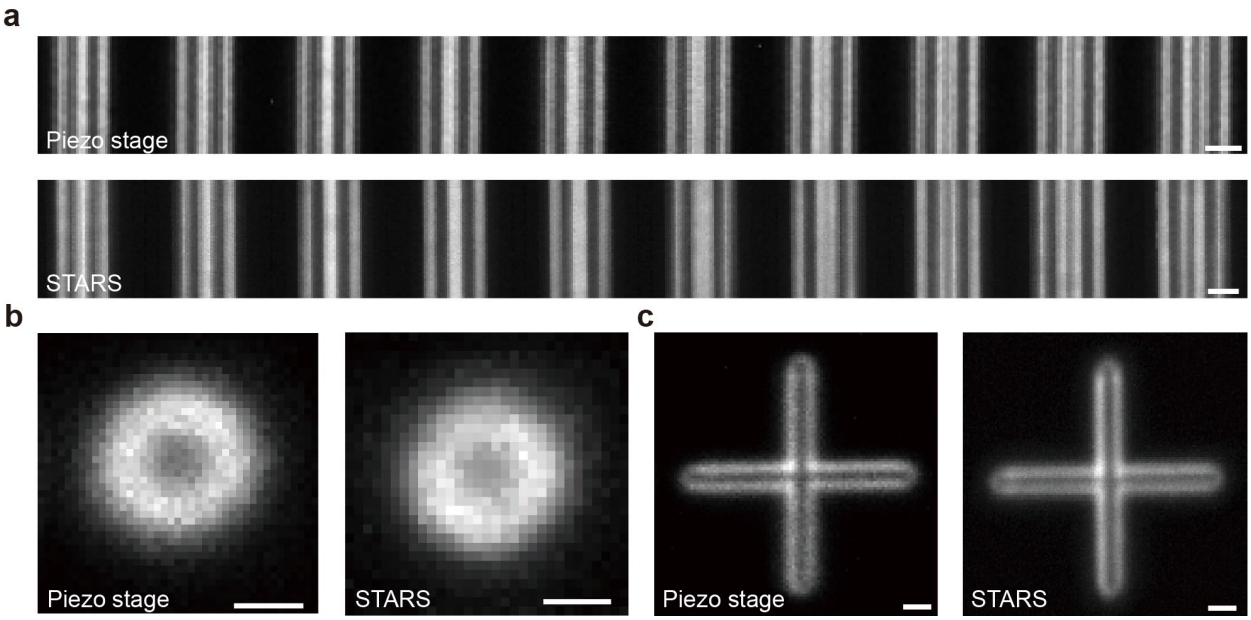
Supplementary Figure 2. Workflow for offline photon-based volumetric reconstruction. The FPGA records three parameters for each photon event: the arrival time stamp, the EOD scanning index, and the TAG phase. The EOD index (1-121) corresponds to a unique (x, y) coordinate, allowing reconstruction of the lateral photon distribution. The TAG lens performs sinusoidal axial scanning, and the z position of each photon is determined from the TAG phase. Because the scanning velocity is lower near the turning points, photons accumulate at the axial extremes, producing intensity enhancement. To correct this bias, the intensity of each axial layer is normalized by the corresponding laser dwell time, compensating for the non-uniform sampling induced by the sinusoidal TAG scan.

Langtaosha (LTS) Preprint doi: https://doi.org/10.65215/LTSpreprints.2026.11.24.000400. This version posted November 24, 2026. The copyright holder for this preprint (which was not certified by peer review) is the author/funder. Creative Commons license: CC Attribution-NonCommercial-NoDerivatives 4.0 https://creativecommons.org/licenses/by-nc-nd/4.0



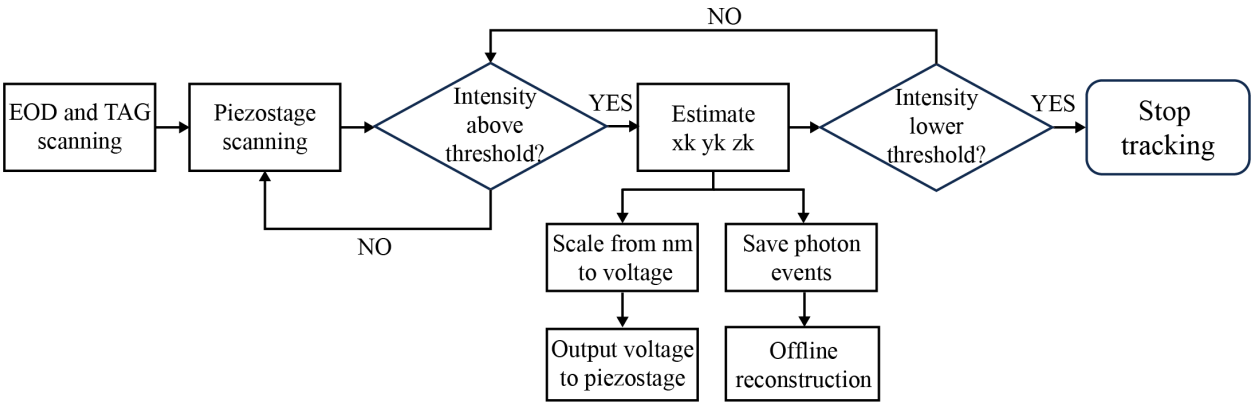
Supplementary Figure 3. Simulation data and reconstruction results. (a) Original fluorescent microsphere dataset. **(b)** The result of PSF convolution applied to the data in (a), using a PSF of 300 nm in xy and 900 nm in z. **(c)** FWHM along the x, y, and z directions for a single microsphere in (b). **(d)** FWHM along the x, y, and z directions for a single microsphere after reconstruction.

Langtaosha (LTS) Preprint doi: https://doi.org/10.65215/LTSpreprints.2026.11.24.000400. This version posted November 24, 2026. The copyright holder for this preprint (which was not certified by peer review) is the author/funder. Creative Commons license: CC Attribution-NonCommercial-NoDerivatives 4.0 https://creativecommons.org/licenses/by-nc-nd/4.0



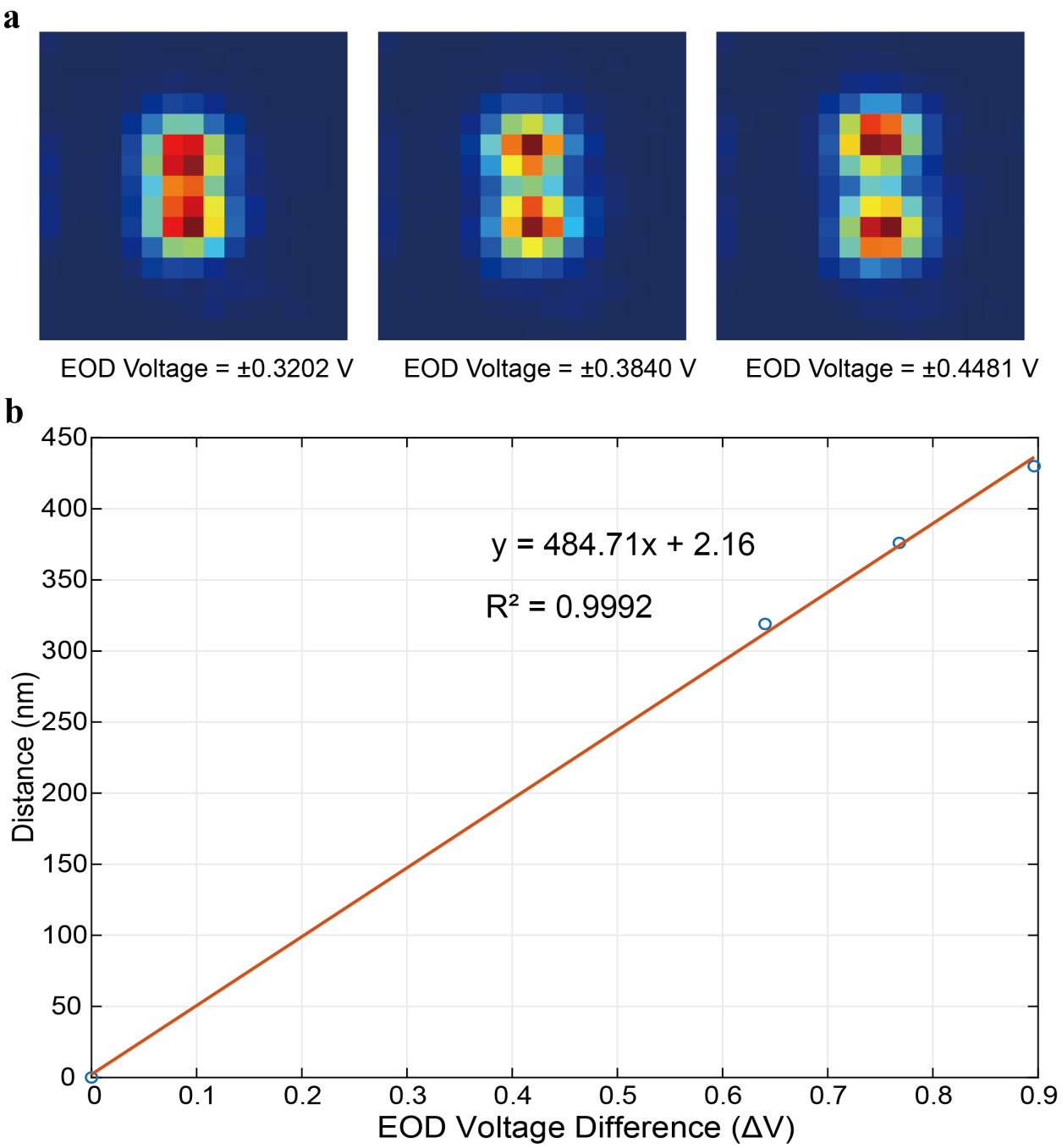
Supplementary Figure 4. Argolight calibration patterns, including line (a), hollow-ring (b) and cross (c) patterns, acquired by stage scanning and STARS. Scale bars: 1 μm.

Langtaosha (LTS) Preprint doi: https://doi.org/10.65215/LTSpreprints.2026.11.24.000400. This version posted November 24, 2026. The copyright holder for this preprint (which was not certified by peer review) is the author/funder. Creative Commons license: CC Attribution-NonCommercial-NoDerivatives 4.0 https://creativecommons.org/licenses/by-nc-nd/4.0



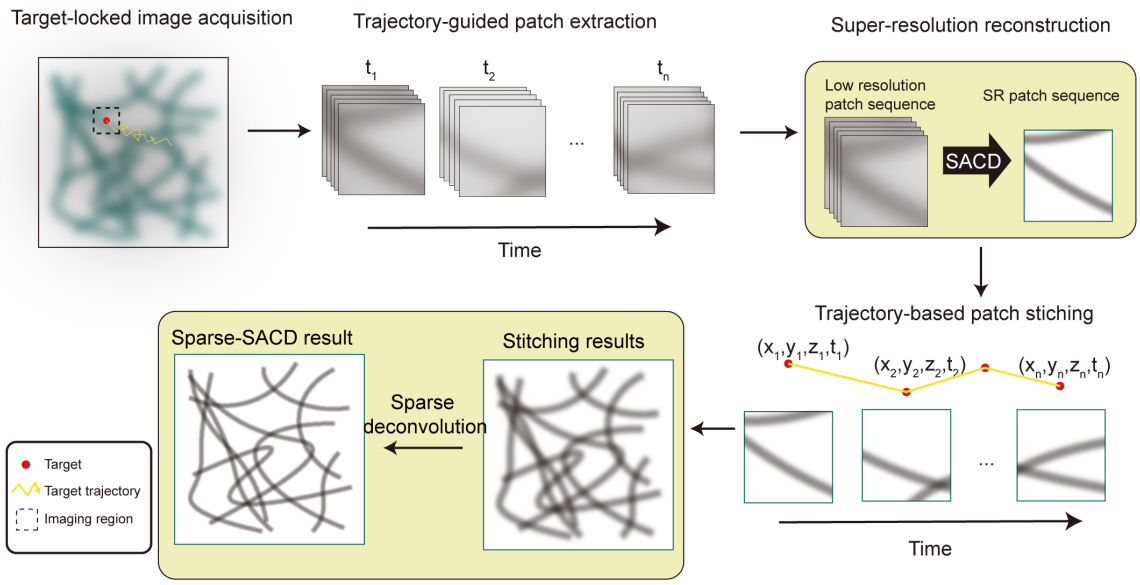
Supplementary Figure 5. The workflow of the STARS system. Through the customised LabVIEW programme, the control system tracks and acquires photon information. The system tracks particles by updating positional estimates, converting them to voltage signals to control the piezo stage, and recording the piezo stage positions and photon events.

Langtaosha (LTS) Preprint doi: https://doi.org/10.65215/LTSpreprints.2026.11.24.000400. This version posted November 24, 2026. The copyright holder for this preprint (which was not certified by peer review) is the author/funder. Creative Commons license: CC Attribution-NonCommercial-NoDerivatives 4.0 https://creativecommons.org/licenses/by-nc-nd/4.0



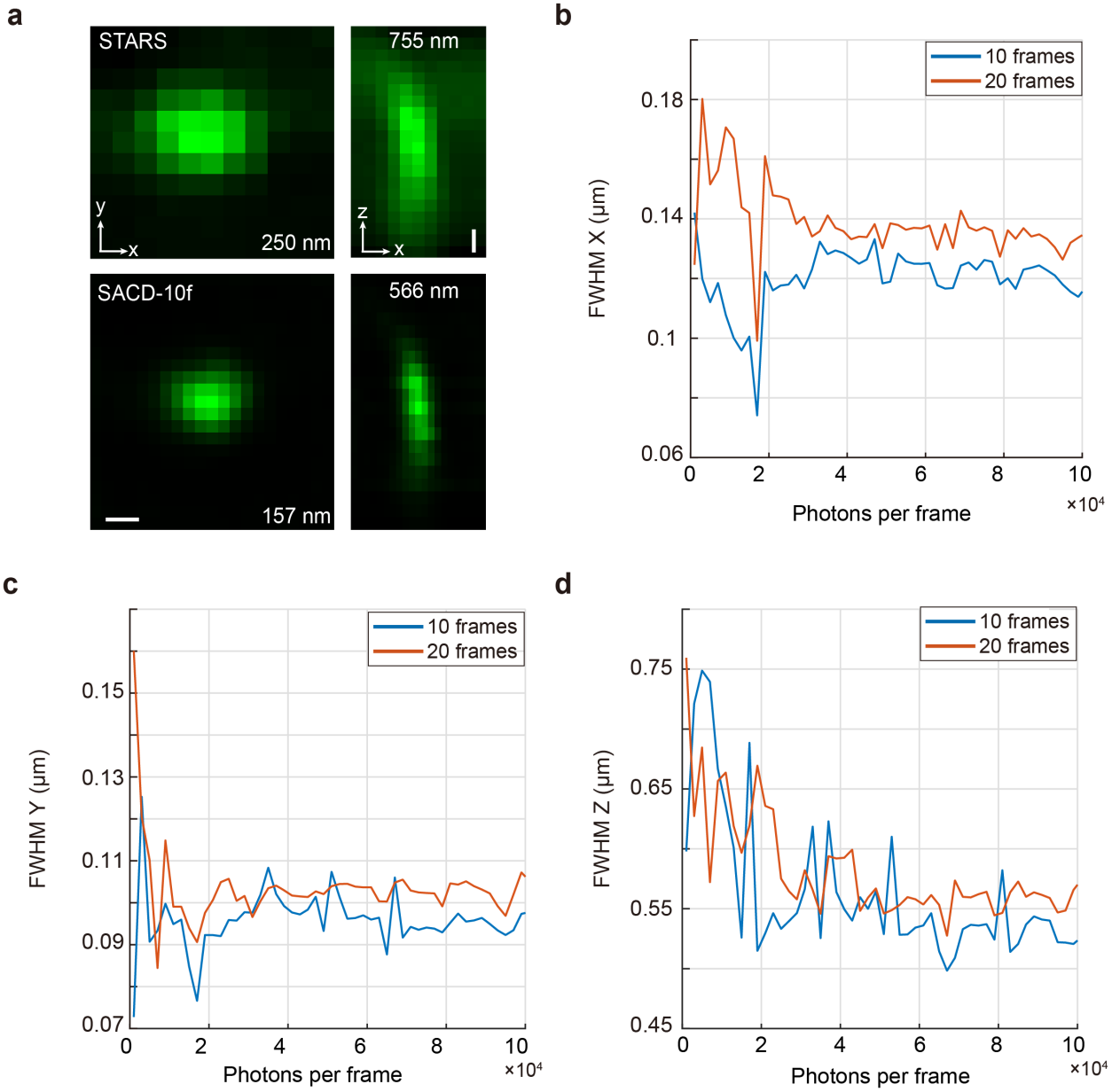
Supplementary Figure 6. EOD Voltage-Distance Calibration. (a) Imaging of 100-nm fluorescent microspheres at different EOD voltages. **(b)** The EOD voltage difference–distance function fitted from the data in (a). The zero-voltage condition was defined as zero displacement, whereas the measured voltage difference–distance relationship was empirically fitted using an unconstrained linear model.

Langtaosha (LTS) Preprint doi: https://doi.org/10.65215/LTSpreprints.2026.11.24.000400. This version posted November 24, 2026. The copyright holder for this preprint (which was not certified by peer review) is the author/funder. Creative Commons license: CC Attribution-NonCommercial-NoDerivatives 4.0 https://creativecommons.org/licenses/by-nc-nd/4.0



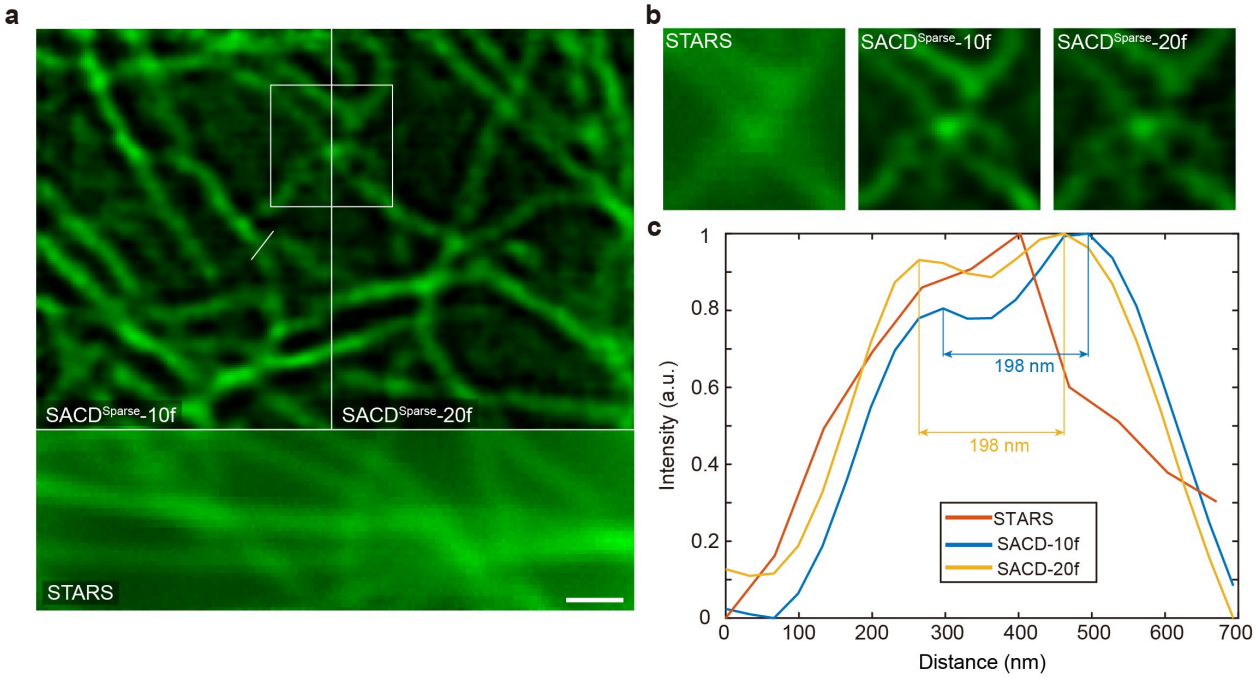
Supplementary Figure 7. Workflow of Sparse-SACD for improving the reconstruction resolution of STARS. Target-locked image data are divided into trajectory-guided local patches. Temporal image sequences for each patch are processed with SACD. The reconstructed patches are then registered using the recorded target coordinates and stitched along the trajectory. Sparse deconvolution is applied to the stitched reconstruction to generate the final Sparse-SACD image.

Langtaosha (LTS) Preprint doi: https://doi.org/10.65215/LTSpreprints.2026.11.24.000400. This version posted November 24, 2026. The copyright holder for this preprint (which was not certified by peer review) is the author/funder. Creative Commons license: CC Attribution-NonCommercial-NoDerivatives 4.0 https://creativecommons.org/licenses/by-nc-nd/4.0



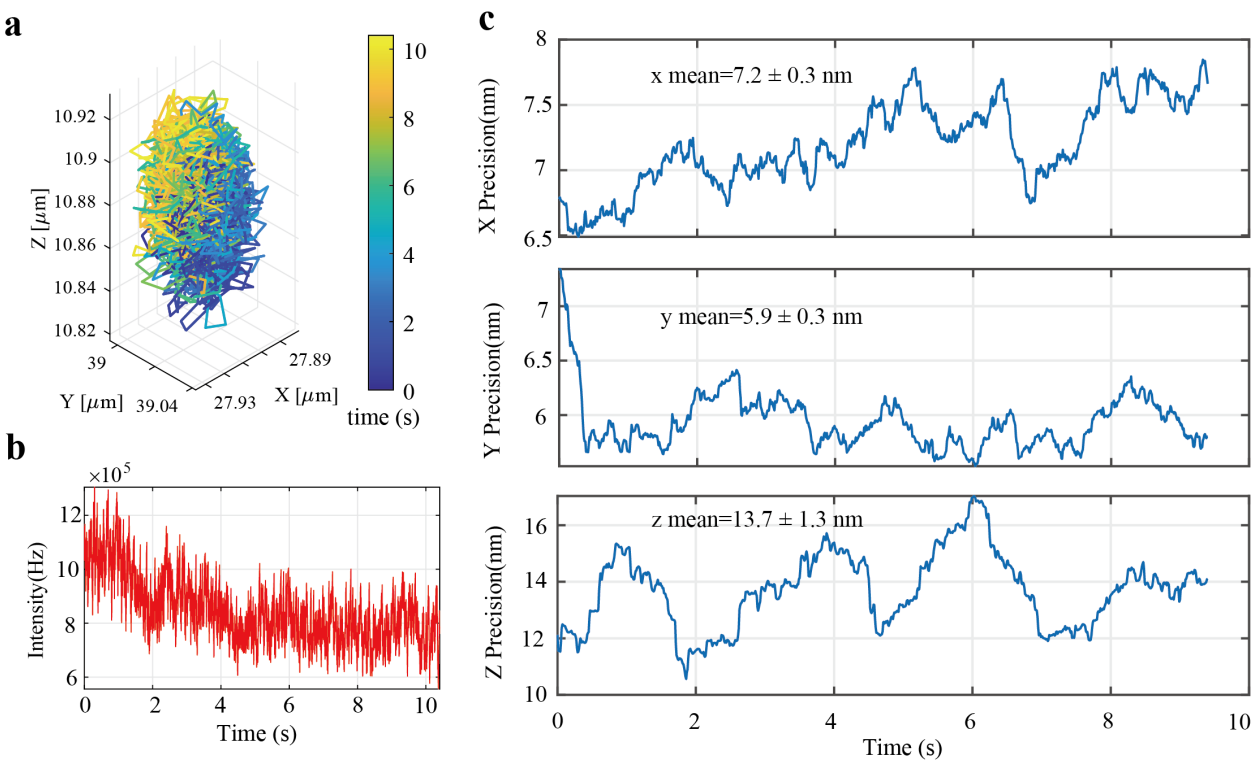
Supplementary Figure 8. Photon-number dependence of spatial resolution enhancement by Sparse-SACD. (a) Maximum intensity projections in the xy plane (left) and corresponding xz cross-sections (right) of a single fluorescent bead reconstructed by STARS (top) and Sparse-SACD using 10-frame data (bottom). The measured lateral and axial full width at half-maximum (FWHM) values are indicated. Scale bar, 100 nm. **(b–d)** FWHM values measured along the x (b), y (c), and z (d) directions as a function of the detected photon number. Blue and orange curves represent results obtained from 10-frame and 20-frame datasets, respectively, with an integration time of 0.1 s per frame.

Langtaosha (LTS) Preprint doi: https://doi.org/10.65215/LTSpreprints.2026.11.24.000400. This version posted November 24, 2026. The copyright holder for this preprint (which was not certified by peer review) is the author/funder. Creative Commons license: CC Attribution-NonCommercial-NoDerivatives 4.0 https://creativecommons.org/licenses/by-nc-nd/4.0



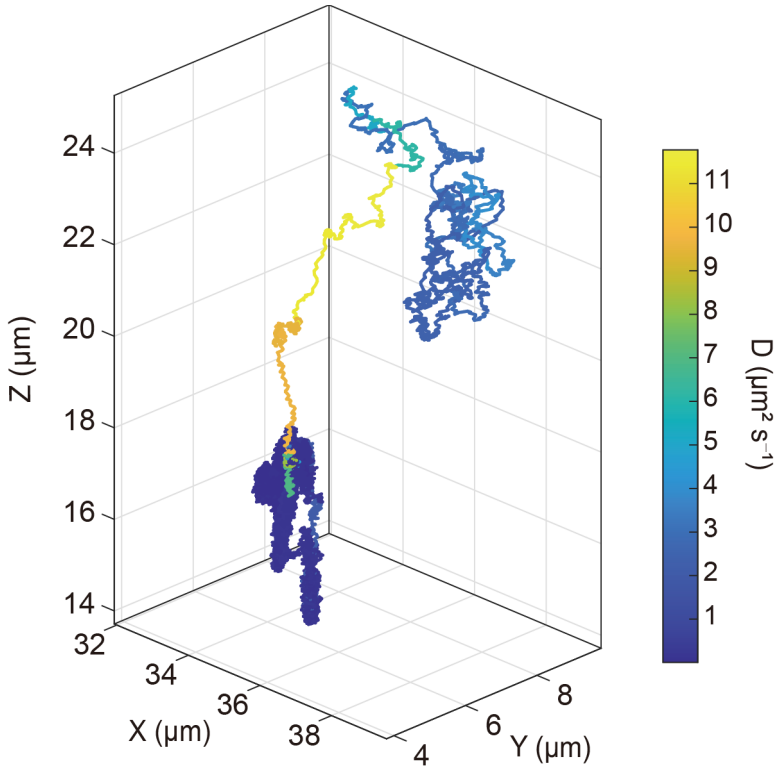
Supplementary Figure 9. Comparison of Sparse-SACD reconstruction using 10-frame and 20-frame datasets for microtubule imaging. (a) Maximum-intensity projections of microtubule structures reconstructed using STARS, Sparse-SACD reconstruction using 10 frames, and Sparse-SACD reconstruction using 20 frames. Scale bar: 1 μm. **(b)** Magnified views of the white-boxed region in (a). **(c)** Intensity profiles along the white line indicated in (a). Scale bar: 500 nm.

Langtaosha (LTS) Preprint doi: https://doi.org/10.65215/LTSpreprints.2026.11.24.000400. This version posted November 24, 2026. The copyright holder for this preprint (which was not certified by peer review) is the author/funder. Creative Commons license: CC Attribution-NonCommercial-NoDerivatives 4.0 https://creativecommons.org/licenses/by-nc-nd/4.0



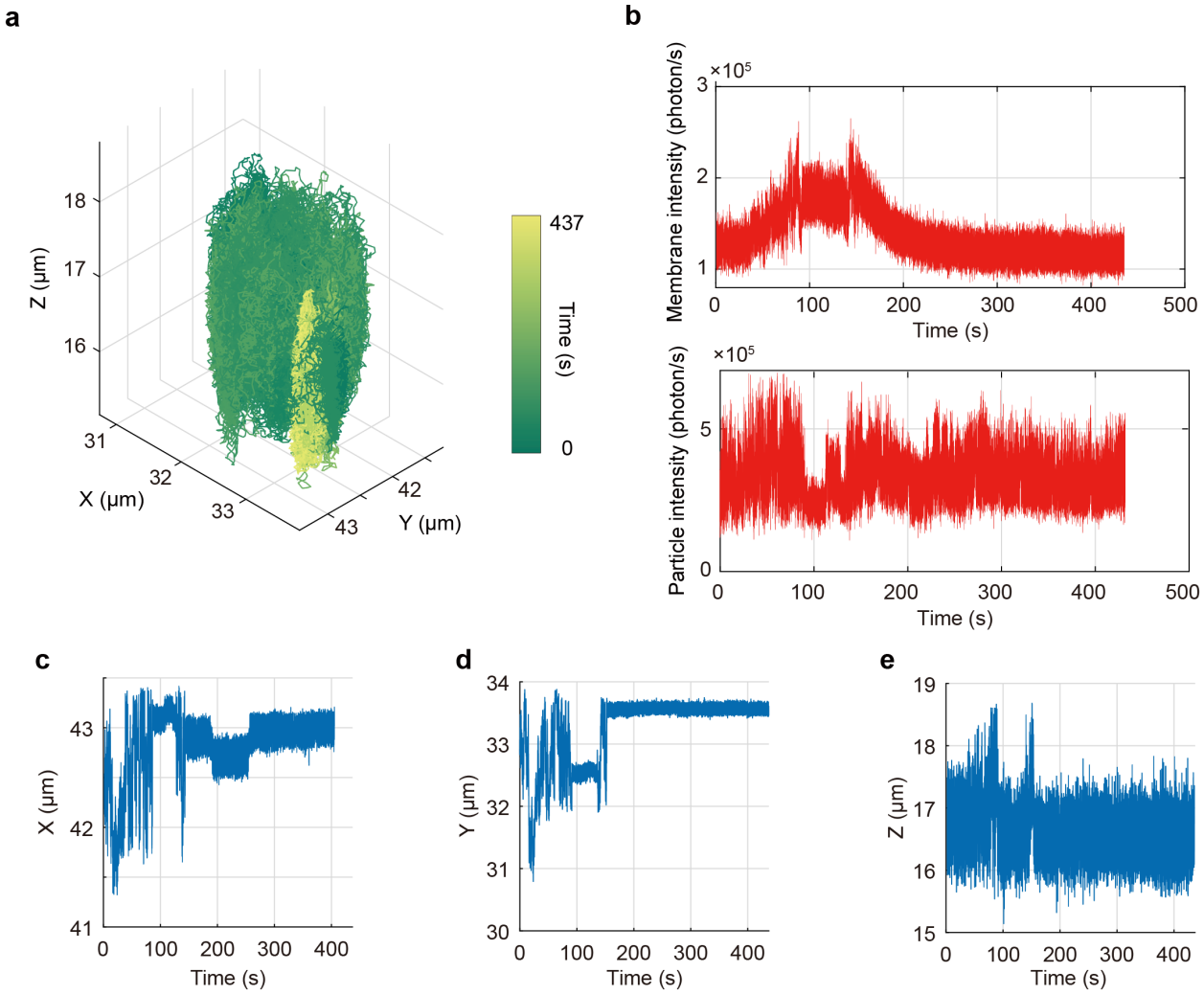
Supplementary Figure 10. Positional precision during three-dimensional tracking. (a) Three-dimensional trajectory of an immobilized 100-nm fluorescent bead, colored by elapsed time. **(b)** Fluorescence intensity as a function of time. **(c)** Time-dependent tracking precision along x, y and z (top to bottom), quantified as the standard deviation of bead positions within 1-s windows advanced in 10-ms increments. The values reported in the plots are 7.2 ± 0.3 nm (x), 5.9 ± 0.3 nm (y) and 13.7 ± 1.3 nm (z).

Langtaosha (LTS) Preprint doi: https://doi.org/10.65215/LTSpreprints.2026.11.24.000400. This version posted November 24, 2026. The copyright holder for this preprint (which was not certified by peer review) is the author/funder. Creative Commons license: CC Attribution-NonCommercial-NoDerivatives 4.0 https://creativecommons.org/licenses/by-nc-nd/4.0



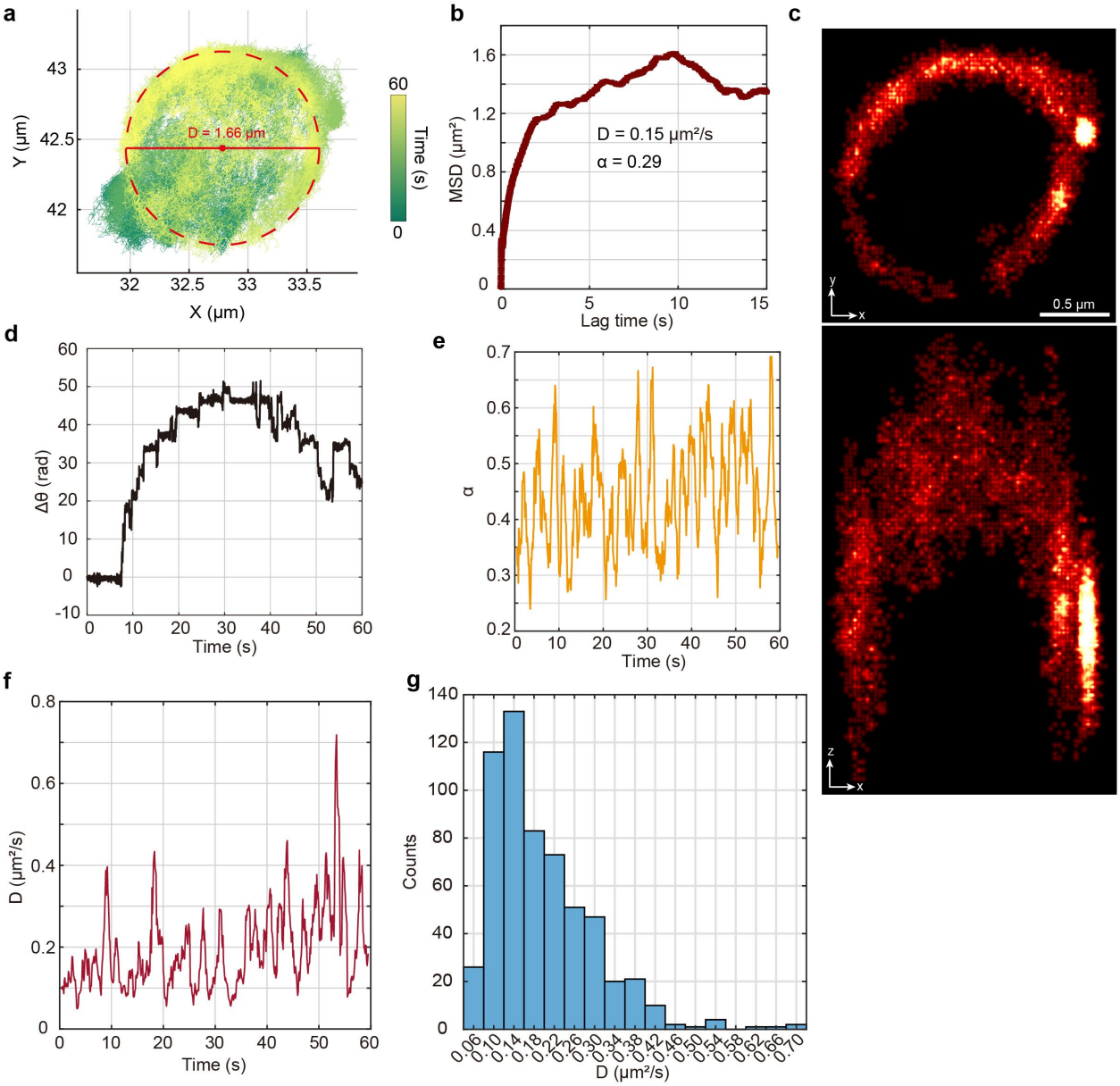
Supplementary Figure 11. Three-dimensional trajectory of a fluorescent bead landing to the cell membrane colored by the apparent diffusion coefficient. The apparent diffusion coefficient was calculated using a 1-s sliding window with a step size of 0.1 s and assigned to the trajectory position corresponding to the temporal midpoint of each window.

Langtaosha (LTS) Preprint doi: https://doi.org/10.65215/LTSpreprints.2026.11.24.000400. This version posted November 24, 2026. The copyright holder for this preprint (which was not certified by peer review) is the author/funder. Creative Commons license: CC Attribution-NonCommercial-NoDerivatives 4.0 https://creativecommons.org/licenses/by-nc-nd/4.0



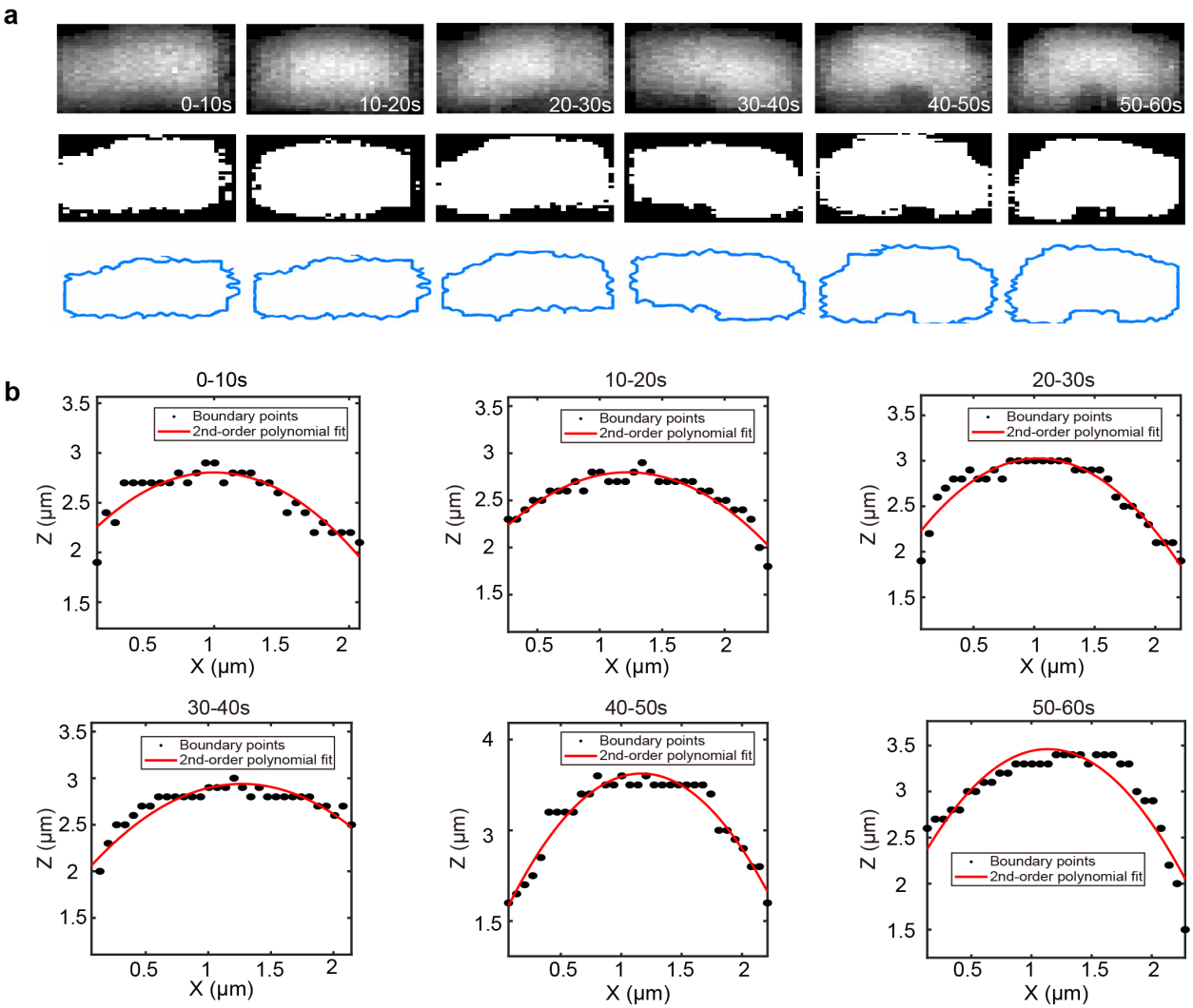
Supplementary Figure 12. Complete trajectory of a silver nanoparticle during cellular membrane protrusion. (**a**) Three-dimensional trajectory of the AgNP recorded during the membrane protrusion process. The trajectory is color-coded according to the recording time. The 60-s trajectory segment shown in **Fig. 2j-l** corresponds to the time interval from 30 s to 90 s of the full recording. **(b)** Temporal variation of the fluorescence intensity of the cell membrane (top) and AgNP signal intensity (bottom) during the entire recording period. **(c–e)** Time-dependent trajectories of the AgNP along the x, y, and z axes, respectively.

Langtaosha (LTS) Preprint doi: https://doi.org/10.65215/LTSpreprints.2026.11.24.000400. This version posted November 24, 2026. The copyright holder for this preprint (which was not certified by peer review) is the author/funder. Creative Commons license: CC Attribution-NonCommercial-NoDerivatives 4.0 https://creativecommons.org/licenses/by-nc-nd/4.0



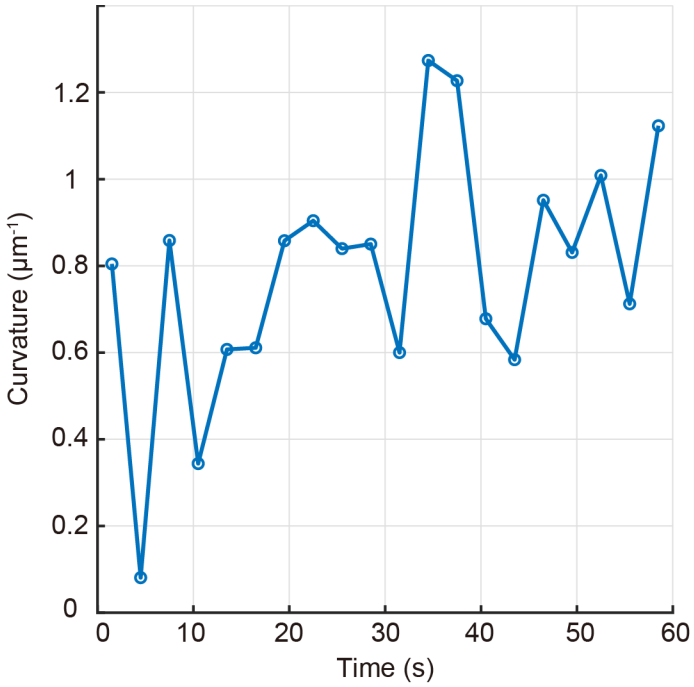
Supplementary Figure 13. Quantitative analysis of the rotational dynamics of an AgNP trajectory during membrane protrusion. (a) Projection onto the xy plane of the AgNP trajectory. A three-dimensional spherical fit of the trajectory yields a characteristic trajectory diameter of approximately 1.66 μm. The trajectory is color-coded according to acquisition time. **(b)** Mean-squared displacement (MSD) analysis of the complete AgNP trajectory. **(c)** Residence-time-weighted spatial projections of the AgNP trajectory onto the xy (top) and xz (bottom) planes, centered on the fitted trajectory center. Only the final 30 s of the 60-s trajectory are shown. The spatial density of trajectory localizations reflects the relative residence time of the AgNP at different positions along the trajectory. **(d)** Temporal evolution of the rotation angle of the AgNP trajectory. **(e)** Time-dependent anomalous diffusion exponent (α) calculated from sliding-window MSD analysis using a 1-s window with a 0.1-s step size. **(f)** Time-dependent diffusion coefficient (D) extracted from the same sliding-window MSD analysis. **(g)** Distribution of diffusion coefficients obtained from the sliding-window trajectory analysis.

Langtaosha (LTS) Preprint doi: https://doi.org/10.65215/LTSpreprints.2026.11.24.000400. This version posted November 24, 2026. The copyright holder for this preprint (which was not certified by peer review) is the author/funder. Creative Commons license: CC Attribution-NonCommercial-NoDerivatives 4.0 https://creativecommons.org/licenses/by-nc-nd/4.0



Supplementary Figure 14. Extraction and polynomial fitting of the membrane boundary during protrusion formation. (a) Image processing workflow for membrane boundary extraction from reconstructed protrusion images across consecutive 10-s time windows (0–10, 10–20, 20–30, 30–40, 40–50, and 50–60 s). The upper row shows the reconstructed fluorescence images, the middle row shows the corresponding binary masks generated by threshold segmentation, and the bottom row presents the extracted membrane boundaries. **(b)** Second-order polynomial fitting of the extracted membrane boundary points for each 10-s time window. The black dots represent the detected boundary points, and the red curves indicate the fitted membrane profiles obtained using a second-order polynomial model.

Langtaosha (LTS) Preprint doi: https://doi.org/10.65215/LTSpreprints.2026.11.24.000400. This version posted November 24, 2026. The copyright holder for this preprint (which was not certified by peer review) is the author/funder. Creative Commons license: CC Attribution-NonCommercial-NoDerivatives 4.0 https://creativecommons.org/licenses/by-nc-nd/4.0



Supplementary Figure 15. Temporal evolution of the average curvature of the projected membrane contour during protrusion formation. The average curvature was calculated from second-order polynomial-fitted boundary profiles extracted from reconstructed XZ images at 3-s intervals. The average curvature increases overall during protrusion formation, reflecting progressive membrane deformation.

Langtaosha (LTS) Preprint doi: https://doi.org/10.65215/LTSpreprints.2026.11.24.000400. This version posted November 24, 2026. The copyright holder for this preprint (which was not certified by peer review) is the author/funder. Creative Commons license: CC Attribution-NonCommercial-NoDerivatives 4.0 https://creativecommons.org/licenses/by-nc-nd/4.0

Supplementary Table 1. Optical path configurations and experimental parameters.

Experiments	Laser and Power (measured after objective lens)	F1 filter	F2 filter	F3 filter
Fluorescent beads tracking and imaging	Green beads, 488 nm: 0.1 μW	525/50(ET525/50m,Chroma)	-	-
Nanosilver tracking and lysosomal imaging	AgNP,488 nm:1.82 μW 638 nm:0.71μW	-	-	706/95(ET706/95 m, Chroma)
Nanosilver tracking and microtubule imaging	AgNP,488 nm: 1.82 μW 638 nm: 0.71μW	-	-	706/95(ET706/95 m, Chroma)
Fluorescent beads tracking and cell membrane imaging	Green beads, 488 nm: 0.1 μW 638 nm: 0.71μW	-	-	706/95(ET706/95 m, Chroma)
Cell membrane protrusion imaging	AgNP,488 nm: 1.82 μW 638 nm: 0.71μW	-	-	706/95(ET706/95 m, Chroma)